





## Article

# Sol–Gel-Process-Based Molten-Flux Synthesis of Plate-like $\text{La}_2\text{NiO}_{4+\delta}$ Particles

Giamper Escobar Cano , Yannick Brinkmann, Zhijun Zhao , Patrick A. Kießling  and Armin Feldhoff 

Institute of Physical Chemistry and Electrochemistry, Leibniz University Hannover, Callinstr. 3A, D-30167 Hannover, Germany

\* Correspondence: [giamper.escobar@pci.uni-hannover.de](mailto:giamper.escobar@pci.uni-hannover.de) (G.E.C.); [armin.feldhoff@pci.uni-hannover.de](mailto:armin.feldhoff@pci.uni-hannover.de) (A.F.)

**Abstract:**  $\text{La}_2\text{NiO}_{4+\delta}$  particles with a plate-like morphology were prepared from a NaOH melt by molten-flux synthesis. For this purpose, the intermediates from a sol–gel process were used as reactants. Using powder X-ray diffraction, the sol–gel intermediates were identified as a mixture of tetragonal  $\text{La}_2\text{O}_2\text{CO}_3$  and cubic NiO. The existence of NiO was also confirmed by transmission electron microscopy in combination with electron-energy loss spectroscopy. The ultrafine mixed sol–gel intermediates were then mixed with NaOH powder and additional water in a nickel crucible and heated to 673 K for 8 h. The chemical reactions in the air during the molten-flux synthesis and the influence of the salt on the formation of  $\text{La}_2\text{NiO}_{4+\delta}$  were examined by thermogravimetric analysis. The powder X-ray diffraction indicated a  $\text{K}_2\text{NiF}_4$ -type tetragonal structure with the  $I4/mmm$  space group for the reaction product. The scanning electron microscopy showed plate-like  $\text{La}_2\text{NiO}_{4+\delta}$  crystals with a length and thickness of approximately 9  $\mu\text{m}$  and 2  $\mu\text{m}$ , respectively, while the energy-dispersive X-ray spectroscopy revealed a homogeneous distribution of lanthanum and nickel in the product powder. The influence of the processing parameters on the product generation, as well as on the size and morphology of the  $\text{La}_2\text{NiO}_{4+\delta}$  particles, was systematically studied.



**Citation:** Escobar Cano, G.; Brinkmann, Y.; Zhao, Z.; Kießling, P.A.; Feldhoff, A. Sol–Gel-Process-Based Molten-Flux Synthesis of Plate-like  $\text{La}_2\text{NiO}_{4+\delta}$  Particles. *Crystals* **2022**, *12*, 1346. <https://doi.org/10.3390/cryst12101346>

Academic Editors: Faheem Ahmed, Nishat Arshi, Shalendra Kumar and Nagih Shaalan

Received: 5 September 2022

Accepted: 17 September 2022

Published: 24 September 2022

**Publisher's Note:** MDPI stays neutral with regard to jurisdictional claims in published maps and institutional affiliations.



**Copyright:** © 2022 by the authors. Licensee MDPI, Basel, Switzerland. This article is an open access article distributed under the terms and conditions of the Creative Commons Attribution (CC BY) license (<https://creativecommons.org/licenses/by/4.0/>).

**Keywords:** crystal growth; crystal morphology;  $\text{La}_2\text{NiO}_{4+\delta}$ ; molten-flux synthesis; NaOH melt; sol–gel process

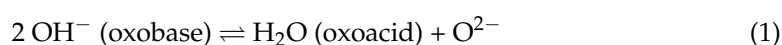
## 1. Introduction

Due to its high chemical and thermal stability in a  $\text{CO}_2$ -containing atmosphere under working conditions, the mixed ionic–electronic conductor (MIEC) oxide  $\text{La}_2\text{NiO}_{4+\delta}$  (LNO) has attracted considerable attention in the research area of oxygen-transporting membranes (OTMs) [1]. OTMs based on MIECs find applications in the production of oxygen-enriched air, the partial oxidation of methane to syngas or ethane to ethylene and as cathode material in solid-oxide fuel cells (SOFCs) or in lithium–air batteries [2–7]. LNO exhibits a  $\text{K}_2\text{NiF}_4$  structure and is the first member ( $n = 1$ ) of the Ruddlesden–Popper (RP) phase series, which can be generally described by the formula  $\text{La}_{n+1}\text{Ni}_n\text{O}_{3n+1}$  ( $n = 1, 2, 3, \infty$ ). The crystal structure of LNO is anisotropic and consists of alternating cubic perovskite  $\text{LaNiO}_3$  layers and  $\text{LaO}$  rock-salt layers along its  $c$ -axis [8–10]. The rock-salt layers are able to include oxygen ions in interstitial positions, which are involved in the oxygen-transport mechanism in LNO [9]. The migration of oxygen ions through LNO is highly anisotropic and occurs mainly in the  $ab$  plane of the structure [11,12]. The amount of the oxygen interstitials can be described by the oxygen excess  $\delta$ . Depending on the  $\delta$  ( $0 \leq \delta \leq 0.25$ ) and temperature, LNO can exhibit versatile orthorhombic and tetragonal structures [13–16].

LNO is typically prepared by the sol–gel process (SGP) implicating reactions between nanocrystalline intermediates, which require high temperatures of at least 1223 K to obtain pure powder product with crystal sizes up to a few micrometers [1,17–20]. However, the crystal morphology of the resulting LNO particles cannot be controlled by the SGP [17–20]. As an alternative method, molten-flux synthesis (MFS) enables the production of anisotropic

metal-oxide materials, such as LNO, with high purity. The chemical conversion during MFS takes place in a liquid medium, resulting in the faster mobility of the ionic species compared to the SGP. This leads to the high homogeneity of the reaction mixture, and the synthesis can be completed in shorter times. Furthermore, the MFS permits the formation of large crystals, mostly in the micrometer range, and well-defined morphologies according to the crystal structure. Depending on the flux used, and thus, its melting point, MFS usually requires a lower reaction temperature than the SGP [21–26].

For the investigations in this study, NaOH was chosen as the flux due to its low melting point of 596 K [27]. It has previously been reported that the use of the stronger oxidant KOH compared with NaOH causes the production of the perovskite-like oxide  $\text{LaNiO}_3$ . The presence of peroxides and superoxides in the KOH melt stabilizes the +3 oxidation state of Ni, facilitating the exclusive formation of  $\text{LaNiO}_3$  [28]. Analogous to the autoprotolysis of water, and according to the Lux–Flood theory [29], the acid–base equilibrium present in the NaOH melt can be described as follows:



The MFS starts with the dissolution of the reactants in the wet acidic melt. The heating of the reaction mixture causes a slow loss of water, making the melt more basic and promoting product formation by shifting the acid–base equilibrium. The basicity of the melt is expressed analogously to the pH value as a function of the oxygen ions in the following way:

$$p\text{O}^{2-} = -\log [\text{O}^{2-}] \quad (2)$$

where  $p\text{O}^{2-}$  is the potential of the oxygen ions, and  $[\text{O}^{2-}]$  corresponds to the concentration of the oxygen ions. The possible chemical reactions in the melt are determined by the magnitude of the  $p\text{O}^{2-}$  [30–32]. Analogous to the introduction of the absolute pH scale [33], Equation (2) can be related to the absolute chemical potential of the oxygen ions ( $\mu_{\text{O}^{2-}, \text{abs}}$ ), according to Equation (3):

$$p\text{O}_{\text{abs}}^{2-} = -\mu_{\text{O}^{2-}, \text{abs}} / RT \ln 10 \quad (3)$$

Here,  $R$  is the gas constant, and  $T$  is the temperature. This definition allows us to compare the basicity of the oxygen ions in different chemical environments. So far, many materials, such as  $\text{La}_{2-x}\text{M}_x\text{CuO}_4$  ( $M = \text{Na}, \text{K}$ ),  $\text{LnBa}_2\text{Cu}_3\text{O}_{7-\delta}$  ( $\text{Ln} = \text{Nd}, \text{Sm}, \text{Eu}, \text{Gd}$ ) and  $\text{LnCu}_2\text{O}_4$  ( $\text{Ln} = \text{La}, \text{Nd}, \text{Sm}, \text{Eu}, \text{Gd}, \text{Dy}, \text{Ho}, \text{Y}, \text{Er}$ ), have been successfully synthesized via MFS using a NaOH–KOH eutectic [34–36]. The use of pure NaOH as a flux in MFS has only been reported in a few cases. For example,  $\text{LnFeO}_3$  ( $\text{Ln} = \text{La}, \text{Pr}, \text{Nd}$ ) and  $\text{Na}_{0.2}\text{CoO}_2$  were obtained from a NaOH melt [37,38]. In earlier work, plate-like LNO crystals were synthesized by MFS using NaOH as the flux. Nevertheless, in addition to LNO, the secondary phase  $\text{La}(\text{OH})_3$  was also identified, which can represent an obstacle for possible future applications due to its size of at least  $10 \mu\text{m}$  [39,40]. LNO plates, obtained via solid-state route-mediated MFS, have already been used in our research group to fabricate the ceramic composite from  $\text{Ca}_3\text{Co}_{4-x}\text{O}_{9+\delta}$  and a small amount of LNO (max. 5 wt%), which showed enhanced thermoelectric properties compared to pure  $\text{Ca}_3\text{Co}_{4-x}\text{O}_{9+\delta}$  [41]. Due to the anisotropic crystal structure and oxygen-transport properties, LNO particles with a plate-like shape can possibly be used as template particles for the production of microstructured LNO ceramic membranes with increased oxygen-transport rates using a templated grain-growth process [40,42]. Thermogravimetric analysis (TGA) investigations on the oxygen uptake/release of nanostructured LNO materials have previously demonstrated that LNO with a rod-like geometry, prepared via the reversible microemulsion method, led to a 75% increase in the oxygen-transport rates compared with LNO to a polyhedral shape [43].

In this work, the synthesis of plate-like LNO particles by the molten-flux method with NaOH as the flux is reported. An ultrafine mixture of intermediates consisting of  $\text{La}_2\text{O}_2\text{CO}_3$  and NiO from the SGP was used as the precursor. By the appropriate choice of the reaction parameters, high-purity micron-sized LNO was produced. A number of

different analytical methods were utilized to characterize the sol–gel intermediates and LNO product powder.

## 2. Materials and Methods

The reactants for the MFS of LNO were synthesized by the SGP using  $\text{La}(\text{NO}_3)_3 \cdot 6 \text{H}_2\text{O}$  (Alfa Aesar, Kandel, Germany, 99.9%) and  $\text{Ni}(\text{NO}_3)_2 \cdot 6 \text{H}_2\text{O}$  (Alfa Aesar, Kandel, Germany, 99.9%) as metal precursors, ethylenediaminetetraacetic acid (EDTA) (Alfa Aesar, Kandel, Germany, 99.4%) and citric acid (Alfa Aesar, Kandel, Germany, 99.5%). Stoichiometric amounts of the metal precursors were dissolved in distilled water at 353 K. EDTA and citric acid were added under stirring until the molar ratio of  $\text{La}^{3+}:\text{Ni}^{2+}:\text{EDTA}:\text{citric acid}$  was 2:1.15:3.15:6.3. After adjusting the pH value between 7 and 9 by adding  $\text{NH}_3 \cdot \text{H}_2\text{O}$  (Carl Roth, Karlsruhe, Germany,  $\geq 25\%$ ), a blue-colored sol was formed. The solution was then heated at 423 K for a few hours under constant stirring until a blue gel was obtained. Next, the gel was transferred to an evaporating dish and heated in a heating mantle for several hours at 573 K. After complete water evaporation, a xerogel powder was obtained, which was thoroughly ground and then calcined in air in a furnace at 773 K for 2 h using a heating and cooling rate of 2 K/min. The finely mixed sol–gel intermediates gained in this way were ground and used as starting material for the MFS in the next step.

For a typical MFS, distilled water was first added to NaOH beads (Alfa Aesar, Kandel, Germany, 99.9%) in a nickel crucible. Then, the sol–gel intermediates (La/Ni molar ratio = 2:1.15) were added to the NaOH, resulting in a sol–gel-intermediates/NaOH/ $\text{H}_2\text{O}$ -weight ratio of 1:5:0.9. The crucible was transferred in a muffle furnace and heated at 673 K for 8 h, with a heating rate of 10 K/min and a cooling rate of 2 K/min. After the furnace was cooled to room temperature, the dark-colored crude product was washed several times with distilled water, treated in an ultrasonic bath for a few minutes and filtrated to remove residual NaOH, smaller particles and other impurities. Finally, the product powder was washed with acetone and dried at 373 K.

The crystal structure and phase identification of the reaction products were determined by powder X-ray diffraction (XRD) (Bruker D8 Advance, Bruker AXS GmbH, Karlsruhe, Germany), which was operated at 40 kV and 40 mA using monochromatic  $\text{Cu-K}_\alpha$  radiation. XRD data were collected in a step-scan mode in the  $2\theta$  range of  $10\text{--}50^\circ$ , with a step size of  $0.01^\circ$ , and count times of 1 s per step. Powder diffraction files (PDFs) from the ICDD database were used to identify the following chemical compounds from the recorded XRD patterns:  $\text{La}_2\text{NiO}_4$  (PDF 01-089-3589; tetragonal;  $a = 3.866 \text{ \AA}$ ;  $c = 12.678 \text{ \AA}$ );  $\text{LaNiO}_3$  (PDF 00-033-0710; cubic;  $a = 3.861 \text{ \AA}$ );  $\text{La}(\text{OH})_3$  (PDF 01-079-5398; hexagonal;  $a = 6.529 \text{ \AA}$ ;  $c = 3.852 \text{ \AA}$ );  $\text{La}_2\text{O}_3$  (PDF 01-074-2430; hexagonal;  $a = 3.937 \text{ \AA}$ ;  $c = 6.130 \text{ \AA}$ );  $\text{La}_2\text{O}_2\text{CO}_3$  (PDF 00-023-0320; tetragonal;  $a = 4.063 \text{ \AA}$ ;  $c = 13.500 \text{ \AA}$ ); NiO (PDF 01-071-4750; cubic;  $a = 4.200 \text{ \AA}$ ).

Morphological investigations of the synthesized chemical compounds were performed with a field-emission scanning electron microscope (FE-SEM) (JEOL JSM-6700F, Tokyo, Japan) using a secondary electron detector at 2 kV. The size of the LNO crystals was determined from the recorded SEM micrographs using the image analysis program ImageJ, version 1.53e (Wayne Rasband, U.S. National Institutes of Health, Bethesda, Maryland, USA) [44]. For this purpose, 100 particles were evaluated. The chemical compositions of the sol–gel intermediates and LNO powder were investigated by an energy-dispersive X-ray spectrometer (EDXS) (Oxford Instruments INCA-300, Abingdon, Oxfordshire, UK), with an ultrathin window at 15 kV, located on the SEM. For a more precise determination of the amounts of La and Ni in the reaction products, the oxygen content was omitted, as this chemical element is difficult to quantify exactly by EDXS due to its limited sensitivity.

A field-emission transmission electron microscope (FE-TEM) (JEOL JEM-2100F-UHR, Tokyo, Japan,  $C_s = 0.5 \text{ mm}$  and  $C_c = 1.2 \text{ mm}$ ) in bright-field and high-resolution mode (HRTEM) at 200 kV was used to further characterize the sol–gel intermediates. The microscope was equipped with a Gatan GIF 2001 energy filter and a 1 k charge-coupled-device (CCD) camera to acquire the selected area electron diffraction (SAED) patterns and electron-

energy-loss (EEL) spectra. For the TEM measurements, the powder was placed on a carbon-coated copper TEM grid.

Chemical reactions in the air and the role of the flux during the MFS were studied by TGA and differential thermal gravimetric analysis (DTGA) using a TGA/DSC 3+ from Mettler-Toledo GmbH, Giessen, Germany. For this, the mixtures were transferred into alumina crucibles. The measurements were taken in the temperature range of 298–1073 K, with a heating rate of 10 K/min and a cooling rate of 2 K/min.

### 3. Results and Discussion

#### 3.1. Synthesis of Precursors via Sol–Gel Process

The reactants for the MFS were obtained via the SGP from lanthanum and nickel nitrate using EDTA as the complexing agent and citric acid as the gelation agent. The schematic representation of the SGP is shown in Figure 1. After adding ammonia water to the reaction mixture, a blue sol was formed, which turned into a gel after a few hours through the dehydration and evaporation of ammonia [45,46]. In the next step, the blue-colored gel was heated to 573 K. As a result of the liquid loss, a xerogel powder was produced [47,48]. The powder still contained residues of incompletely burned carbon and nitrogen-based components that could have an impact on the MFS, and they were therefore removed by a calcination step [39]. The calcination of the xerogel powder at 773 K resulted in a crystalline product, hereinafter called sol–gel intermediates.

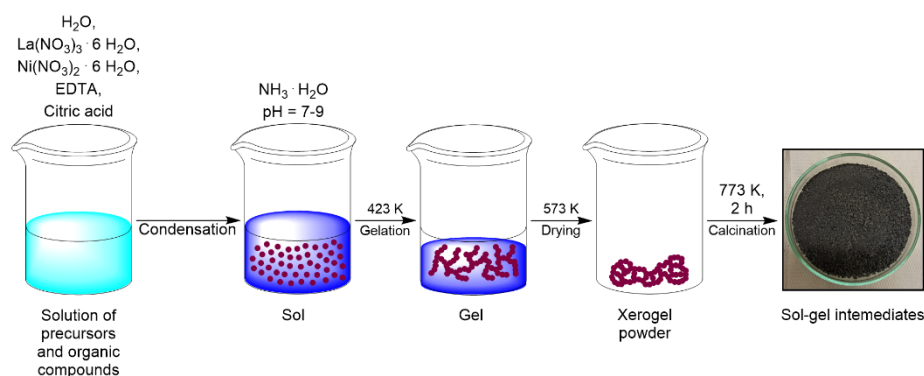
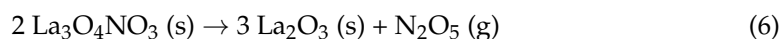
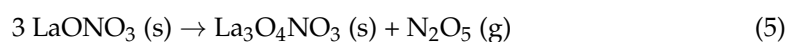
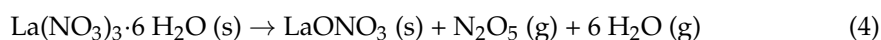


**Figure 1.** Schematic illustration of the preparation of the sol–gel intermediates by the sol–gel process (SGP), which serve as starting material for the molten-flux synthesis (MFS) of  $\text{La}_2\text{NiO}_{4+\delta}$  (LNO).

A calcination temperature of 773 K was chosen because, in previous works, the formation of the first crystalline intermediates,  $\text{La}_2\text{O}_2\text{CO}_3$  and  $\text{NiO}$ , instead of LNO, was observed between 673 K and 773 K [39]. Temperatures between 773 K and 1173 K led to the generation of LNO, accompanied by  $\text{La}_2\text{O}_2\text{CO}_3$  in different phases,  $\text{La}_2\text{O}_3$  and  $\text{NiO}$ . From a temperature of 1223 K or higher, only pure LNO was obtained [17]. The appearance of the intermediate product  $\text{La}_2\text{O}_2\text{CO}_3$  can be explained by the reaction between  $\text{La}_2\text{O}_3$  and atmospheric  $\text{CO}_2$ . Furthermore, the production of this oxycarbonate was favored by the presence of carbonaceous compounds in the reaction mixture, which released  $\text{CO}_2$  when burned.  $\text{La}_2\text{O}_3$  is formed as the result of the decomposition of the lanthanum precursor. The chemical reactions during the combustion of the  $\text{La}(\text{NO}_3)_3 \cdot 6 \text{H}_2\text{O}$  and the formation of lanthanum oxycarbonate can be described by Equations (4)–(7), involving the decomposition of lanthanum oxynitrate species [49]:



It is important to mention that  $N_2O_5$  can decompose into other gaseous products, such as  $NO$ ,  $NO_2$ ,  $NO_3$  or  $O_2$ , depending on the temperature [50]. The stability of  $La_2O_2CO_3$  has been studied elsewhere using an Ellingham diagram, and it was found that this crystalline intermediate compound is not thermodynamically stable above 753 K in ambient air when  $p(CO_2) = 30$  Pa [17]. The presence of lanthanum oxycarbonate in the sol–gel product between 773 K and 1023 K could be attributed to the reaction kinetics, which is supported by the fact that no oxycarbonate was found in the powder gained between 873 K and 1073 K after 20 h [17]. The detection of NiO in the sol–gel intermediates has, so far, proven difficult [17,39]. No sharp NiO reflections could be found by XRD, which means that the NiO particles are too small or still amorphous [39]. Bright-field scanning transmission electron microscopy (STEM) together with EDXS revealed that the product from a SGP at 1023 K and 2 h is an intermixed ultrafine powder composed of individual lanthanum- and nickel-based nanoscale grains with a size below 100 nm [17]. It is therefore possible that NiO particles are nanoparticles, which, depending on their size, lead to a strong broadening of the reflections in the XRD pattern so that they can no longer be distinguished from the background. The mechanism of NiO formation has not yet been elucidated. Possibly, NiO is the product of the decomposition of  $NiCO_3$ . According to the Ellingham diagram,  $NiCO_3$  disintegrates into NiO and  $CO_2$  at a temperature below 773 K, and so this carbonate is no longer found in sol–gel intermediates [17].

For the synthesis of the sol–gel intermediates, a La/Ni molar ratio of 2:1.15 was employed, which, as is discussed later, was conducive to the formation of pure LNO during the MFS. The SEM micrographs in Figure 2 show a porous sponge-like structure generated by the release of gases, such as  $CO_2$  and  $NO_x$ , from the organic and nitrogen-based compounds after the calcination step [51]. The size of the grains is not inferior to 100 nm.

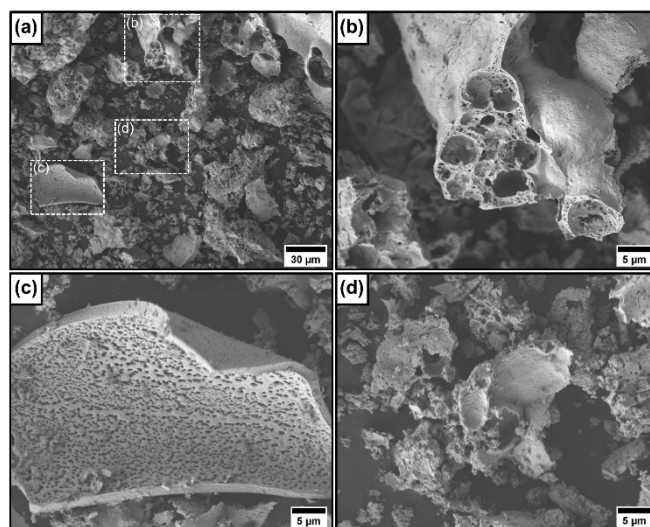


**Figure 2.** Scanning electron microscopy (SEM) micrographs of sol–gel intermediates: (a) overview image, and (b–d) higher magnifications of selected areas in (a) showing that the powder exhibits a porous sponge-structure produced by the release of organic residues and nitrogen oxides.

Next, the chemical composition of the sol–gel intermediates was analyzed via EDXS. In Figure 3a, the area selected for the EDXS study is presented. The EDXS spectrum in Figure 3b displays the presence of La and Ni in the product powder. As can be observed in Figure A1, the EDXS elemental maps reveal highly homogeneous distributions of both metals, and they further confirm that the La/Ni ratio is close to 2:1.15 (see Table 1), which is in good agreement with the stoichiometry of  $La_2O_2CO_3$  and NiO.

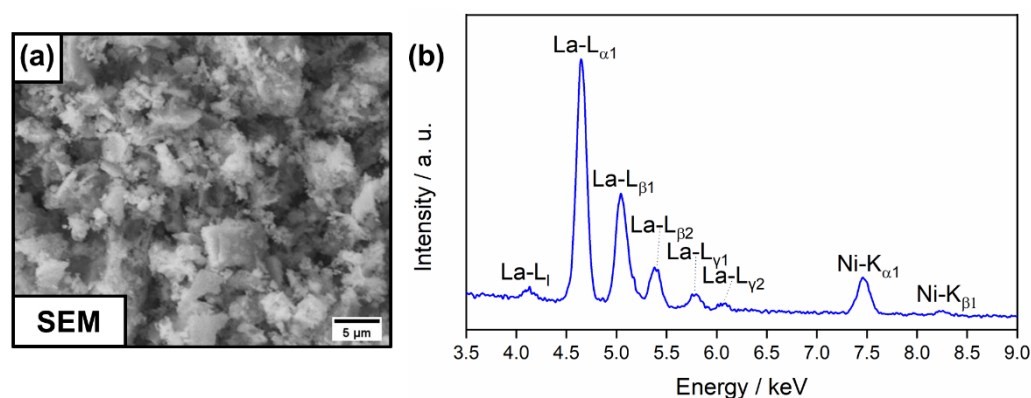


**Figure 3.** Energy-dispersive X-ray spectroscopy (EDXS) analysis of sol–gel intermediates: (a) SEM micrograph showing the area for EDXS analysis; (b) EDXS spectrum exhibiting the presence of La and Ni in the powder. See Figure A1 for more details.

**Table 1.** Metal composition of sol–gel intermediates based on EDXS results.

Element	Atomic Percent (%)	Stoichiometric Ratio <sup>1</sup>
La	66.29 ± 0.28	2.26 ± 0.01
Ni	33.71 ± 0.67	1.15 ± 0.02

<sup>1</sup> Normalized by the atomic percent of Ni.

The EDXS results demonstrated that the SGP produced a mixed ultrafine powder of  $\text{La}_2\text{O}_2\text{CO}_3$  and NiO, which is an excellent precursor for MFS. This high level of mixing is considered to be a common feature and a great advantage of the SGP [17]. In another research work, a mixture of  $\text{La}_2\text{O}_3$  and nanoscale NiO prepared by SSR was utilized for the MFS of LNO [39]. It turned out that the NiO was not homogeneously distributed in the oxide mixture, but it formed agglomerates with sizes of a few micrometers. These inhomogeneities led to the increased formation of the byproducts  $\text{La}(\text{OH})_3$  and  $\text{LaNiO}_3$  during the MFS [39].

XRD measurements of the sol–gel intermediates were also recorded. The XRD pattern displayed in Figure 4 affirms that tetragonal  $\text{La}_2\text{O}_2\text{CO}_3$  and cubic NiO were formed in the powder at 773 K. Compared with previous works, the NiO reflections are visible, which can be partly explained by the higher nickel content in the starting material (La/Ni molar ratio = 1:1.15) [39]. Nevertheless, the NiO reflections are not as pronounced as the lanthanum oxycarbonate reflections, which indicates a NiO particle size in the nanometer range.

For a detailed analysis of the sol–gel intermediates, the powder was examined using bright-field TEM (see Figure 5a). The HRTEM micrographs presented in Figure 5b,c of the selected areas in Figure 5a exhibit the existence of tetragonal  $\text{La}_2\text{O}_2\text{CO}_3$ . The lattice fringes arise from the (002) plane of this oxycarbonate with a distance of 0.62 nm, which agrees with the value of PDF 00-023-0320. NiO and  $\text{La}_2\text{O}_2\text{CO}_3$  were also detected by SAED. As seen in Figure 5d, the SAED pattern manifests polycrystalline Debye–Scherrer rings, which belong to the (002), (101) and (110) planes of tetragonal  $\text{La}_2\text{O}_2\text{CO}_3$ , and to the (111), (200) and (220) planes of cubic NiO (PDF 01-071-475). To gain more information about the composition of the sol–gel intermediates, an EEL spectrum in the low-loss region (see Figure 5e) of a sample area shown in Figure 5a was recorded, demonstrating the plasmon region for NiO, ionization edges of Ni-M<sub>2,3</sub> at 68 eV, and La-N<sub>4,5</sub> in the range of 99–140 eV [52,53]. By comparison with the EEL spectra from other publications and the EELS atlas from Gatan, the NiO could be successfully identified [52–55].

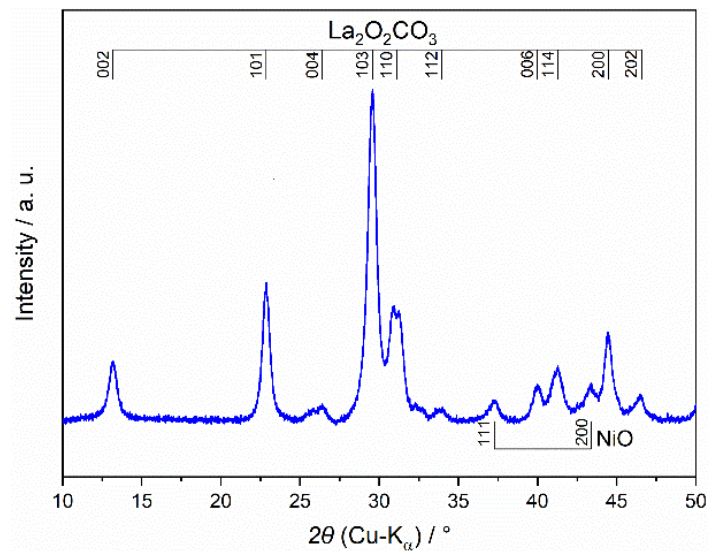


**Figure 4.** Powder X-ray diffraction (XRD) pattern of sol-gel intermediates. The powder consists of  $\text{La}_2\text{O}_2\text{CO}_3$  and NiO. Indexed reflections of tetragonal  $\text{La}_2\text{O}_2\text{CO}_3$  (PDF 00-023-0320) and cubic NiO (PDF 01-071-4750) are indicated by solid lines.

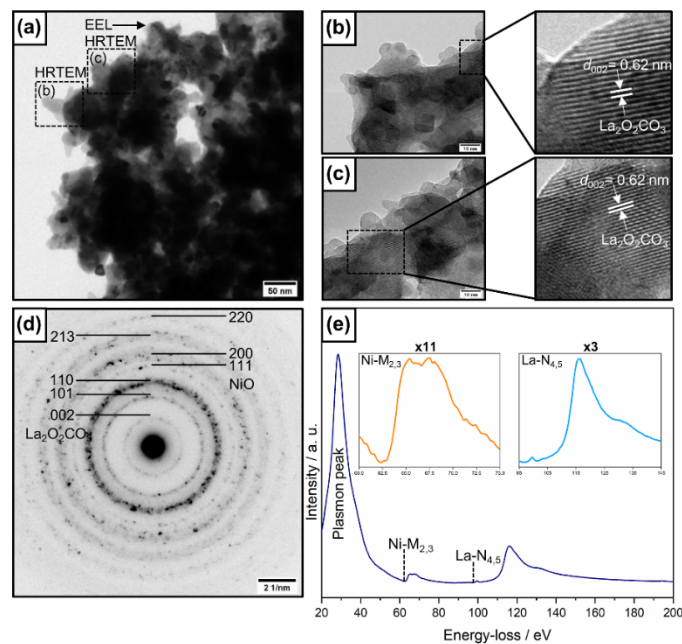


**Figure 5.** Transmission electron microscopy (TEM) characterization of sol-gel intermediates: (a) TEM bright-field micrograph exhibiting the selected region of the product powder for high-resolution TEM (HRTEM) and electron-energy-loss (EEL) spectrum; (b,c) HRTEM micrographs of the marked domains in (a) showing the lattice planes of tetragonal  $\text{La}_2\text{O}_2\text{CO}_3$ ; (d) SAED polycrystalline ring pattern (obtained from a circular plane with a diameter of 1.2  $\mu\text{m}$ ) revealing the presence of tetragonal  $\text{La}_2\text{O}_2\text{CO}_3$  and cubic NiO in the intermediates. The Laue indices of  $\text{La}_2\text{O}_2\text{CO}_3$  (PDF 00-023-0320) and NiO (PDF 01-071-4750) are labeled light blue and orange, respectively; (e) EEL spectrum in the low-loss region demonstrating the presence of two distinct phases based on La and Ni in the sol-gel powder. The insets in (e) show the ionization edges of La and Ni, enlarged for better visibility.

### 3.2. Molten-Flux Synthesis of Plate-like $\text{La}_2\text{NiO}_{4+\delta}$ Particles

For the MFS, the finely mixed sol-gel intermediates were combined with solid NaOH and additional distilled water in a nickel crucible and heated at 673 K for 8 h (see Figure 6a). The entire process can be separated into four steps, as schemed in Figure 6b–d. In the

first step, the sol–gel intermediates dissolve in the wet acid NaOH melt, and in the second step, the diffusion of the free ions ( $\text{La}^{3+}$ ,  $\text{Ni}^{2+}$  and  $\text{CO}_3^{2-}$ ) through the molten flux occurs, resulting in a homogenous reaction mixture. In the next step, the nucleation of the reaction products takes place, accompanied by crystal growth from the nuclei based on Ostwald ripening in the last step [23,25].

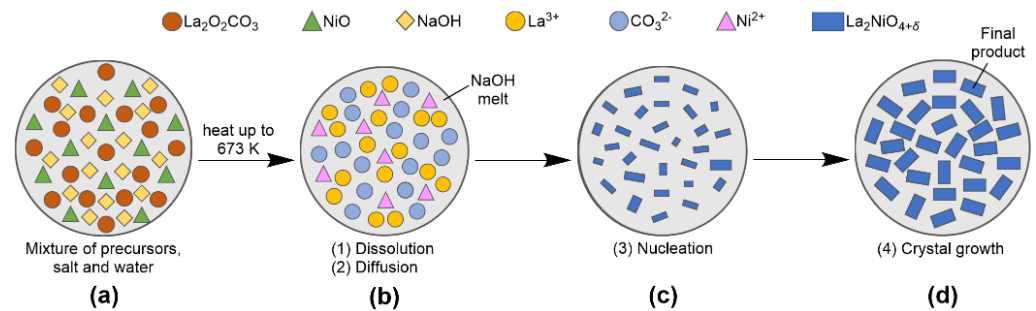
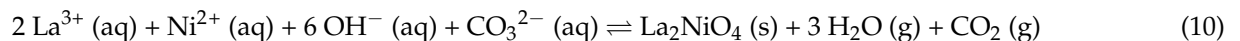
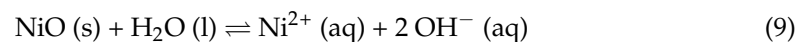
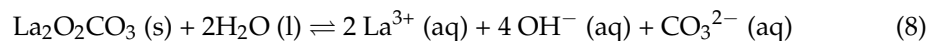


**Figure 6.** Schematic representation of molten-flux process for synthesis of LNO particles using sol–gel intermediates as precursor and NaOH as flux.

The chemical reactions during MFS are given by the following equations [39]:



By adding water, the NaOH melt becomes more acidic. At 596 K, the salt begins to melt, and the sol–gel intermediates dissolve in the resulting wet acidic melt according to Equations (8) and (9). Due to the constant evaporation of water and the release of  $\text{CO}_2$  during the MFS at 673 K, the equilibrium reaction is shifted to the product side (see Equation (10)) so that the target product, LNO, is formed.

The chemical transformations during the MFS in the ambient air and the influence of the flux on the product formation were studied by TGA. For this, the TGA and DTGA curves of the sol–gel intermediates were recorded in the presence or absence of NaOH. Figure 7a displays the thermal decomposition of the sol–gel powder. A weight loss of approximately 30% between 300 K and 650 K was observed after the evaporation of water and the liberation of residual  $\text{CO}_2$  and  $\text{NO}_x$  from the SGP. Above 700 K,  $\text{La}_2\text{O}_2\text{CO}_3$  chemically decomposes, releasing  $\text{CO}_2$ , which leads to a mass loss of about 10%. Finally, LNO is generated from about 900 K [17]. The addition of NaOH to the crystalline intermediates changes the course of the chemical reaction, as can be seen in Figure 7b. First, the loss of water and  $\text{CO}_2$  takes place in accordance with Equation (10), which is accompanied by a minimal mass decrease. At 596 K, the melting of NaOH occurs, followed by the product formation starting at around 673 K. This means that MFS allows for the generation of LNO at a lower temperature compared to the SGP.

In MFS, the choice of the reaction parameters is essential because they not only influence the particle growth and/or morphology, but also control the product formation. Figure 8 summarizes the investigated influence factors on the MFS. While the reaction conditions highlighted in orange regulate the crystal size and/or shape, the parameters accentuated in blue are decisive the product generation. The arrows show that increasing some parameters has a decisive impact on the particle size or product formation. In contrast, the experimental parameters marked in gray play no role in the product generation or particle size or shape, but their correct selection contributes to the better control of the MFS and results in a higher product yield.



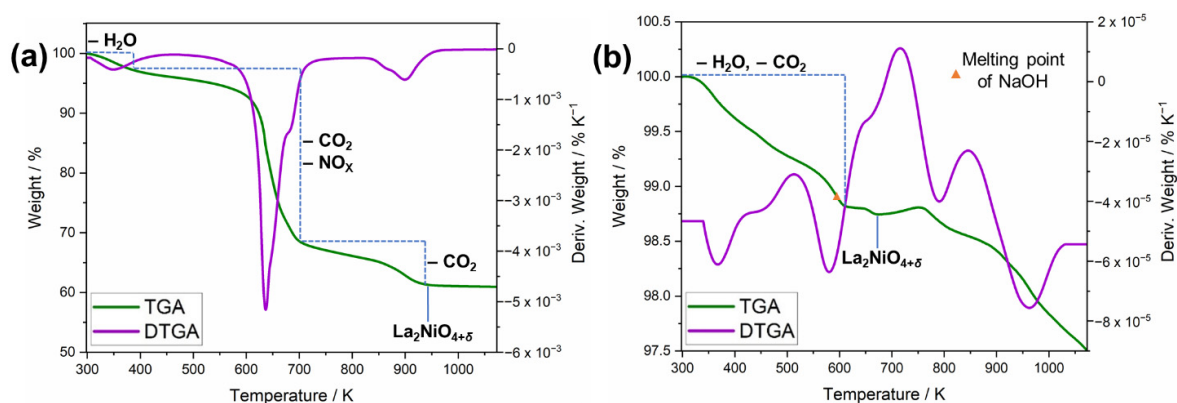


**Figure 7.** Thermogravimetric analysis (TGA) and differential thermal gravimetric (DTGA) of sol-gel intermediates in the presence or absence of the flux: (a) TGA (green) and DTGA (purple) curves of sol-gel powder without NaOH; (b) TGA (green) and DTGA (purple) curves of crystalline intermediates (La/Ni molar ratio = 2:1.15) and NaOH in a 1:10 weight ratio. By adding NaOH, LNO is obtained from 673 K.

**Table 2.** Reaction parameters from the previous scientific publication. Data from [39].

Reaction Parameter	Description/Value
La/Ni molar ratio in the SGI *	2:1
SGI */NaOH-weight ratio	1:10
NaOH/H <sub>2</sub> O-weight ratio	1:0.1
Form of NaOH	Pellets
Crucible material	Al <sub>2</sub> O <sub>3</sub>
Reaction temperature	673 K
Reaction time	8 h
Heating rate	10 K/min
Cooling rate	-

\* SGI: sol-gel intermediates.

The effects of the various reaction parameters on the MFS are explained in more detail below. Only one parameter varied during the investigations, and all the others remained constant. The reaction conditions were adopted from past research work and are listed in Table 2 [39]. The goal of our experiments was to increase the yield of LNO crystals with a well-defined plate morphology while reducing the number of byproducts.

**Form of NaOH:** The use of beads instead of pellets, as in the previous work, has been found to be effective for the following reasons: (i) the beads are of a higher purity (Alfa Aesar, Kandel, Germany, 99.99%) than the NaOH pellets (Carl Roth, Karlsruhe, Germany,  $\geq 99\%$ ); (ii) the beads are smaller ( $\varnothing \leq 1$  mm) than the pellets ( $\varnothing \leq 10$  mm), and are therefore more easily and completely dissolved; (iii) the spherical beads do not react as violently as the other shapes during the MFS, such that the crude product does not spill out of the crucible. The solid form of the flux does not affect the product formation, size or shape, but it allows for a better chemical conversion of the educts and maximizes the product yield.

**Heating and cooling rates:** For other materials obtained via MFS, it was found that the heating and cooling rates do not affect the product formation, but they can control the particle growth [22,56]. Analogous to these investigations, the effects of the heating and cooling processes on the MFS of LNO were studied. Our experiments revealed that the choice of the heating and cooling rates does not influence the product formation or the size and shape of the LNO crystals. Hence, we continued to work with a heating rate of 10 K/min and a cooling rate of 2 K/min, as in [39]. Due to the fast heating rate, the educts and NaOH are brought to the desired reaction temperature in less than one hour, which allows the MFS to be completed in a shorter time.

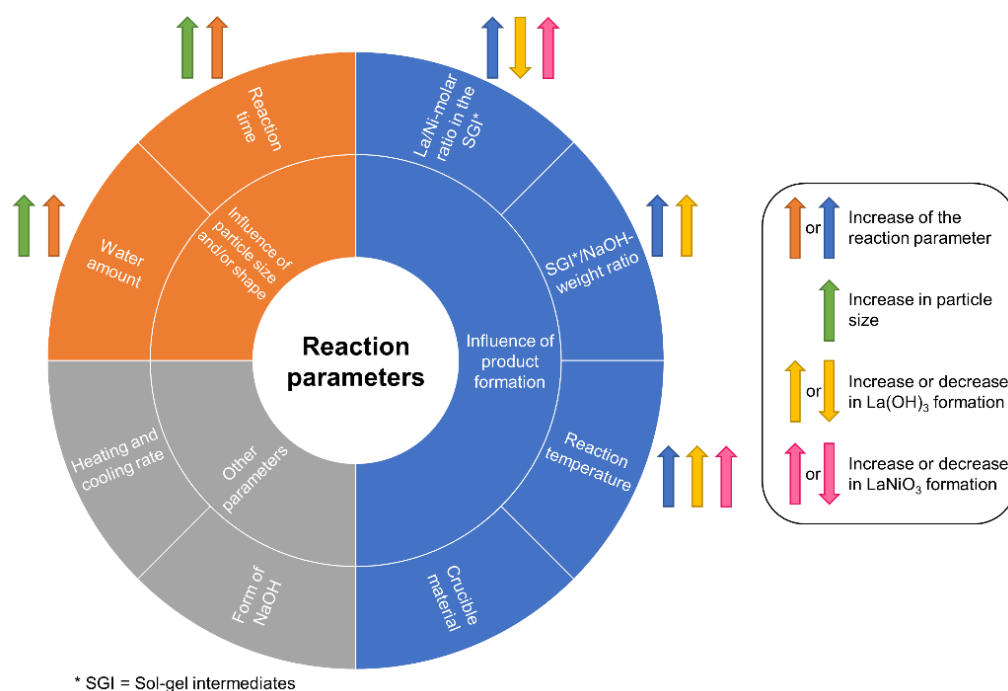


**Figure 8.** Influences of reaction parameters on SGP-based MFS of LNO: sunburst chart illustrating the studied parameters affecting the result of the MFS. See Table 2 for detailed information on the experimental conditions.

**Water amount:** Adding water to solid NaOH creates a wet acidic hydroxide melt (see Equation (1)), which ensures the complete dissolution of the educts. During the MFS, water vapor is expelled from the system, favoring the product formation by shifting the equilibrium position to the right side (see Equation (10)). Compared to the synthesis without additional water, the MFS in the presence of water leads to the production of larger plate-like LNO particles. Without water, LNO crystals with the dimensions of  $3.0 \mu\text{m} \times 0.5 \mu\text{m}$  (length  $\times$  thickness) were found, as shown in Figure A2a. At a NaOH/water-mass ratio of 1:0.1, particles of  $6.0 \mu\text{m} \times 0.7 \mu\text{m}$ , as in Figure A2b, were obtained. Doubling the water content (NaOH/water-weight ratio = 1:0.2) resulted in a further increase in the length to  $9.0 \mu\text{m}$ , and in the thickness to  $0.8 \mu\text{m}$  (see Figure A2c). The formation of larger crystals can be explained by the different nucleation sites and nuclei numbers. The addition of water allows the reactants to dissolve completely when the NaOH melts. At a certain pH value, homogeneous nucleation occurs, resulting in the formation of few nuclei for crystal growth, which favors the formation of larger particles.

**Reaction time:** The SEM micrographs in Figure A3 display the reaction products of the MFS obtained after: (a) 6 h; (b) 8 h; (c) 10 h; (d) 12 h; (e) 18 h at 673 K. After 6 h, many well-defined LNO plates of  $5.0 \mu\text{m} \times 0.6 \mu\text{m}$  could already be observed. Increasing the dwell time to 8 h, 10 h or 12 h was conducive to further but moderate growth, and individual crystals with dimensions of  $6.0 \mu\text{m} \times 0.7 \mu\text{m}$  (8 h),  $6.40 \mu\text{m} \times 0.72 \mu\text{m}$  (10 h) and  $6.80 \mu\text{m} \times 0.74 \mu\text{m}$  (12 h) were won. Choosing a holding time of 18 h led to the formation of very large plate-like structures, some of which were composed of smaller particles. The average length and thickness of the crystals were  $13.0 \mu\text{m}$  and  $1.8 \mu\text{m}$ , respectively. Single plates were found less frequently, suggesting the involvement of the Ostwald ripening process during crystal growth [23,25]. Moreover, longer reaction times increase the flux-loss rate, inducing a higher degree of supersaturation, which benefits particle growth [57].

**Crucible material:** Crucibles composed of  $\text{Al}_2\text{O}_3$ , Ni and Zr were used for the investigations. While the metal crucibles were resistant to molten alkali salts, the alumina melting pot was severely attacked by the NaOH after several syntheses and had to be replaced by another. The XRD patterns presented in Figure A4 demonstrate that utilizing a metal

instead of an  $\text{Al}_2\text{O}_3$  crucible has no effect on the product formation. LNO forms the main phase, and  $\text{La}(\text{OH})_3$  and  $\text{NiO}$  were found as the secondary phases in all the crucibles. The precipitation of  $\text{La}(\text{OH})_3$  can be explained by the reaction of the  $\text{La}^{3+}$  ions with the excess  $\text{OH}^-$  ions, which occurs due to the differences in the solubilities of the reactants. The presence of  $\text{Na}^+$  ions from the flux also favors the  $\text{La}(\text{OH})_3$  formation because  $\text{Na}^+$  can replace  $\text{La}^{3+}$ , and thereby more lanthanum ions are available to fabricate  $\text{La}(\text{OH})_3$  [39]. The observation of  $\text{NiO}$  is due to traces of unreacted nickel oxide from the sol–gel intermediates. Only when using the Ni melting pot was the higher-RP-phase  $\text{LaNiO}_3$  found in the XRD pattern (see Figure A4b), the formation of which could have been caused by the involvement of the crucible in the MFS. However, its contribution should be minor, as Ni as a crucible material remains stable up to 1773 K under the influence of molten  $\text{NaOH}$ , but can already partially react with it to generate  $\text{NiO}$ ,  $\text{Na}_2\text{O}$  and  $\text{H}_2$  from 973 K [58–60]. The SEM micrographs in Figures A3b and A5 show that the plate-shaped LNO particles were obtained, regardless of the crucible chosen. The particles obtained in the  $\text{Al}_2\text{O}_3$  and Ni melting pots were similar in size:  $6.0 \mu\text{m} \times 0.7 \mu\text{m}$  and  $5.5 \mu\text{m} \times 0.5 \mu\text{m}$ , respectively. In contrast, the synthesized plates in the Zr crucible were slightly larger ( $7.00 \mu\text{m} \times 0.72 \mu\text{m}$ ).

**Reaction temperature:** In general, the reaction temperature to form the desired product should be above the melting point of the flux utilized [22,61]. Therefore, molten-flux syntheses were performed at 673 K, 773 K and 873 K. The XRD patterns of the reaction products can be seen in Figure A6. Only at 673 K was LNO identified as the main product, accompanied by a small amount of  $\text{La}(\text{OH})_3$ . Increasing the temperature to 773 K or 873 K led to an increase in the intensity of the  $\text{La}(\text{OH})_3$  reflections. In addition, new byproducts appeared, the reflections of which were assigned to  $\text{LaNiO}_3$ ,  $\text{La}_2\text{O}_3$  and  $\text{NiO}$ . The presence of the oxide  $\text{La}_2\text{O}_3$  can be understood as a result of the thermal decomposition of LNO.  $\text{NiO}$  may originate from the sol–gel intermediates, or as another decomposition product of LNO. Due to the presence of  $\text{NiO}$ , more Ni was available so that the  $\text{LaNiO}_3$  production was favored. On the one hand, the SEM micrographs of the product powders, synthesized at 773 K and 873 K (see Figure A7), display LNO plates of up to  $30 \mu\text{m} \times 2 \mu\text{m}$ . On the other hand,  $\text{La}(\text{OH})_3$  particles of up to  $70 \mu\text{m}$  were found, which could be recognized by their layered hexagonal structure. Temperatures higher than 673 K resulted in larger LNO plates. However, the secondary-phase formation increased unexpectedly. The SEM images revealed that  $\text{La}(\text{OH})_3$  can form even larger structures than LNO, which could pose an issue for potential applications. The optimal formation temperature of LNO by MFS is therefore 673 K.

**Sol–gel-intermediates/ $\text{NaOH}$ -weight ratio:** The amount of flux is critical to the success of the MFS. The salt acts as a solvent and can control the size of the product particles [62,63]. There must be sufficient flux to fill the interstices of the reactant particles and adequately cover the reactant surface. A small quantity of salt cannot ensure the formation of a liquid phase during MFS. Conversely, a high salt mass is not advantageous because it can lead to the separation of the reactant particles by sedimentation. Moreover, excess melted salt may form lumps that are not as easy to dissolve [64]. To examine the influence of  $\text{NaOH}$  on the MFS of LNO, four syntheses were performed using the reactants/ $\text{NaOH}$ -weight ratio: (i) 1:2.5; (ii) 1:5; (iii) 1:7.5; (iv) 1:10. The  $\text{La}(\text{OH})_3$  formation should be minimized by a small content of  $\text{NaOH}$  because there are fewer  $\text{OH}^-$  ions in the melt that can react with the  $\text{La}^{3+}$  ions. The XRD patterns in Figure A8 confirm the presence of LNO, independent of the  $\text{NaOH}$  amount. It can also be observed that  $\text{La}(\text{OH})_3$  was obtained in all four cases. However, up to a sol–gel-intermediates/ $\text{NaOH}$ -weight ratio of 1:5, the amount of  $\text{La}(\text{OH})_3$  was moderate. At a ratio of 1:2.5, the reflections from the LNO were not as sharp, indicating too-small product particles. With higher masses of  $\text{NaOH}$ , the presence of  $\text{La}(\text{OH})_3$  becomes clearer, as the 100 main reflection appears and the intensities of all the other reflections are more pronounced. As can be seen in the SEM images in Figures A3b and A9, LNO particles with the desired morphology were won in all the syntheses. Only at a ratio of 1:2.5 were the LNO plates thin with a rough texture. It is possible that the  $\text{NaOH}$  amount was not high enough, and thus only a small amount of

liquid medium was available for the precursor dissolution and crystal growth. The melt was consumed faster during the MFS due to the constant loss of flux and water, resulting in the formation of smaller product particles with a less well-defined shape. Regardless of the NaOH content, La(OH)<sub>3</sub> was found on all the SEM micrographs. Consequently, a sol–gel-intermediate/NaOH-weight ratio of 1:5 was selected for later investigations.

**La/Ni molar ratio in sol–gel intermediates:** To test the influence of the La/Ni molar ratio in the sol–gel intermediates on the MFS of LNO, reaction mixtures with La/Ni ratios of 2:1; 1.95:1 and 2:1.15 were used. A smaller La amount in the precursor can be advantageous because fewer La<sup>3+</sup> ions are available to react with the OH<sup>−</sup> ions from the flux to form La(OH)<sub>3</sub>. The lack of La<sup>3+</sup> ions can be compensated by the Na<sup>+</sup> ions. The doping of the La site by Na in LNO due to the similar radii of La<sup>3+</sup> (116 pm) and Na<sup>+</sup> (121 pm) has already been observed, which can be described by the chemical formula La<sub>2−x</sub>Na<sub>x</sub>NiO<sub>4+δ</sub> ( $x = 0.05$  or  $0.10$ ) [65,66]. By using a higher amount of Ni in the precursor, there are also fewer La<sup>3+</sup> ions for the formation of La(OH)<sub>3</sub>, but this may have the disadvantage of increasing the formation of the Ni-rich phases, such as LaNiO<sub>3</sub> or NiO. As explained in the section on the role of the crucible, a La/Ni molar ratio of 2:1 in the precursor gave LNO as the main phase. However, La(OH)<sub>3</sub> was identified as a minor phase. As can be seen from the XRD pattern in Figure A10a, a lower amount of La in the sol–gel intermediates reduced the formation of La(OH)<sub>3</sub> partially, but not completely. An increase in the Ni amount in the precursor also led to less La(OH)<sub>3</sub> in the product powder (see Figure A10b). On the contrary, LaNiO<sub>3</sub> perovskite was found, the formation of which can be attributed to the increased amount of Ni used in the precursor. No changes in the morphologies of the resulting LNO plates (see SEM images in Figures A3b and A11) were detected by varying the La/Ni ratio. In short, a lower La amount or higher Ni content in the sol–gel intermediates favors the formation of the main product. Compared with a La/Ni molar ratio of 2:1, the production of La(OH)<sub>3</sub> was reduced, which was evident from the weaker reflections in the XRD pattern.

By the proper choice of the La/Ni molar ratio in the precursor, the precursor/NaOH-weight ratio, and crucible material, the formation of undesirable phases, such as La(OH)<sub>3</sub> and LaNiO<sub>3</sub>, can be specifically decreased so that the main-phase LNO is gained in a high yield. Our experiments have shown that a La/Ni molar ratio in the sol–gel intermediates of 2:1.15, a sol–gel-intermediates/NaOH-mass ratio of 1:5 and the use of a nickel crucible are conducive to the generation of high-purity LNO. In addition, excess water was added to the reaction mixture in order to produce larger crystals. Replacing a Ni crucible with a Zr crucible or an Al<sub>2</sub>O<sub>3</sub> crucible resulted in an increasing amount of La(OH)<sub>3</sub> in the order Ni < Zr < Al<sub>2</sub>O<sub>3</sub>, but it also led to a slight decrease in the LaNiO<sub>3</sub> formation in the order Ni > Zr > Al<sub>2</sub>O<sub>3</sub>, as supported by the XRD. No differences were found in the morphologies of the LNO particles. La(OH)<sub>3</sub> and LaNiO<sub>3</sub> were recognized due to their hexagonal and cubic shapes, respectively (see Figure 9). All the reaction parameters optimized by our investigations are described in Table 3.

XRD measurements, presented in Figure 10, were performed to determine the reaction products of the MFS. For a better understanding, the XRD patterns of the powders prepared under the reaction conditions of the previous publication (see Figure 10a and Table 2) and present work (see Figure 10b and Table 3) are compared. In both cases, LNO was identified as the main phase, which is present in the body-centered tetragonal crystal structure of the K<sub>2</sub>NiF<sub>4</sub> type (space group: *I4/mmm*). This structure is to be expected at temperatures above 423 K (here, 773 K) in air [14,67]. As shown in Figure 10a, using the reaction parameters from Table 2 led to the appearance of hexagonal La(OH)<sub>3</sub> (space group: *P6<sub>3</sub>/m*) and cubic LaNiO<sub>3</sub> (space group: *Pm $\bar{3}$ m*) as impurities. Traces of cubic NiO (space group: *Fm $\bar{3}$ m*) were also found. By optimizing the reaction conditions, it was possible, in this work, to completely suppress the formation of La(OH)<sub>3</sub>, as no further reflections of this product were observed in the XRD patterns in Figure 10b. However, reflections of LaNiO<sub>3</sub> and NiO were still detected, which can be explained by the high content of Ni used in the sol–gel intermediates and the possible participation of the Ni crucible in the reaction.

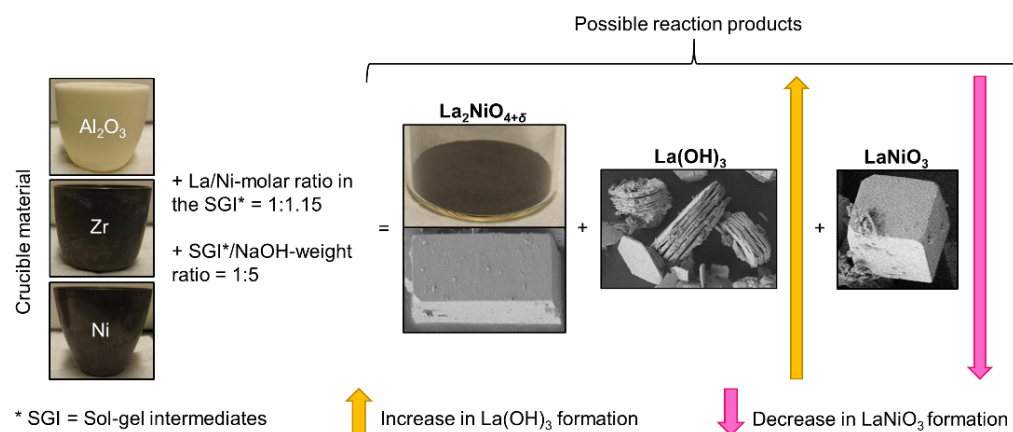


**Figure 9.** The choice of reaction conditions is crucial for product formation. The picture shows the different crucible materials utilized ( $\text{Al}_2\text{O}_3$ , Zr and Ni), which, together with a La/Ni molar ratio in the sol–gel intermediates of 1:1.15 and a sol–gel-intermediates/NaOH-weight ratio of 1:5, led to the formation of LNO as the main phase, as well as  $\text{La}(\text{OH})_3$  and  $\text{LaNiO}_3$  as secondary phases, in different amounts. The morphologies of the different products can be clearly seen from the SEM micrographs: LNO forms plate-like particles,  $\text{La}(\text{OH})_3$  is characterized by its hexagonal structure and  $\text{LaNiO}_3$  has a cubic shape.

**Table 3.** Optimized reaction conditions for the MFS of LNO.

Reaction Parameter	Description/Value
La/Ni molar ratio in SGI *	2:1.15
SGI */NaOH-weight ratio	1:5
NaOH/ $\text{H}_2\text{O}$ -weight ratio	1:0.2
Form of NaOH	Beads
Crucible material	Ni
Reaction temperature	673 K
Reaction time	8 h
Heating rate	10 K/min
Cooling rate	2 K/min

\* SGI: sol–gel intermediates.

The SEM micrographs of the reaction powder, synthesized by MFS under the reaction conditions of Table 2, are displayed in Figure 11. The LNO crystals possess a plate-like morphology, with a size of up to 30  $\mu\text{m}$ . The byproduct  $\text{La}(\text{OH})_3$  was also visible on the SEM images as large crystals with a length of up to 40  $\mu\text{m}$  due to its layered hexagonal structure. The  $\text{La}(\text{OH})_3$  formation should be avoided, as these particles can later interfere, for example, in the fabrication of LNO membranes by reason of their large size.

As can be perceived from the SEM images presented in Figure 12, the application of the reaction conditions of this research in the MFS also resulted in the acquisition of LNO particles, which exhibit a well-defined plate-like shape. The crystals have an average length and thickness of approximately 9  $\mu\text{m}$  and 2  $\mu\text{m}$ , respectively, and thus an aspect ratio close to 5. Because neither  $\text{La}(\text{OH})_3$  nor  $\text{LaNiO}_3$  crystals were found on the SEM micrographs, it can be assumed that the molten-flux method using NaOH induces the formation of high-purity LNO.

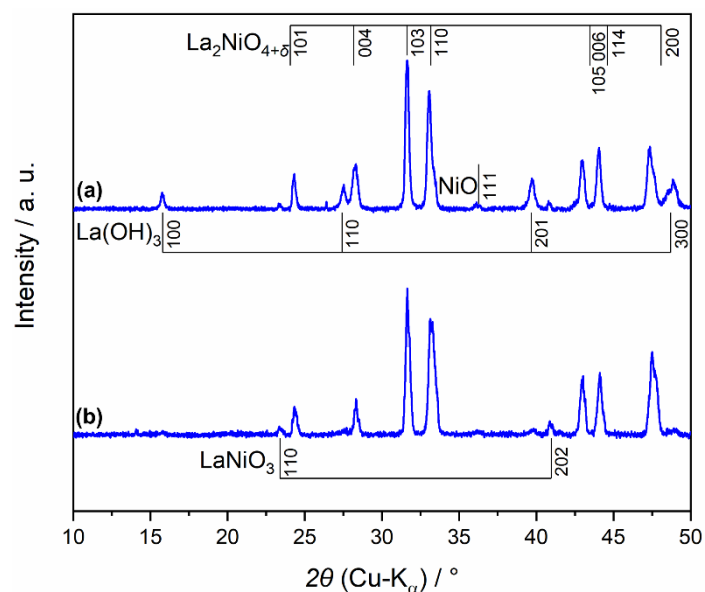


**Figure 10.** Powder XRD patterns of chemical products, obtained by SGP-based MFS: (a) under reaction conditions of Table 2, and (b) from this work (see Table 3 for full details on the reaction parameters). Reflections of the main-product body-centered tetragonal LNO (PDF 01-089-3589) and the minor phases hexagonal  $\text{La}(\text{OH})_3$  (PDF 01-079-5398), cubic  $\text{LaNiO}_3$  (PDF 00-033-0710) and cubic NiO (PDF 01-071-4750) are indexed. The XRD data are normalized to the 103 reflection of LNO.

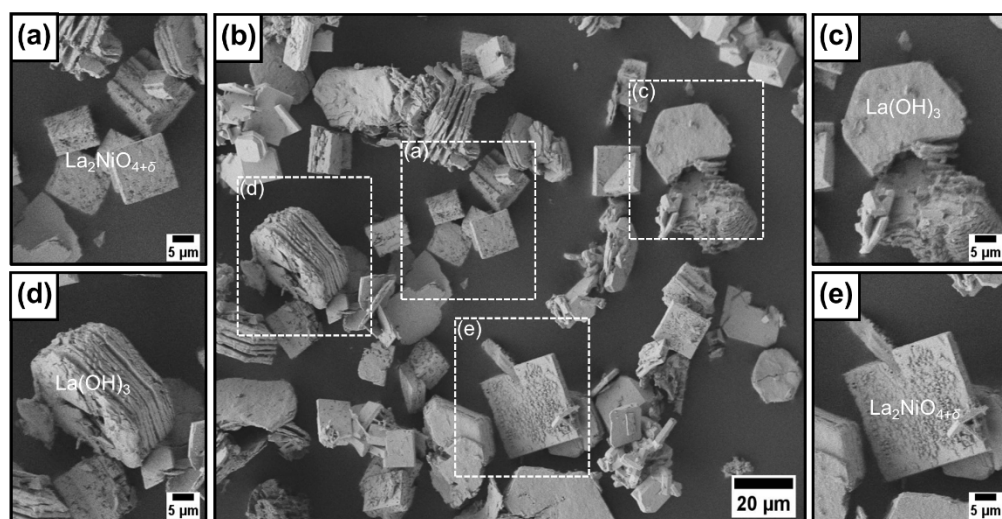


**Figure 11.** SEM micrographs of reaction products, obtained via SGP-based MFS under reaction conditions of Table 2: (a,e) main-product LNO with a plate-like morphology and a length up to 30  $\mu\text{m}$ ; (b) overview of the chemical compounds formed; (c,d) byproduct  $\text{La}(\text{OH})_3$  characterized by a hexagonal layered structure, with a size up to 40  $\mu\text{m}$ .

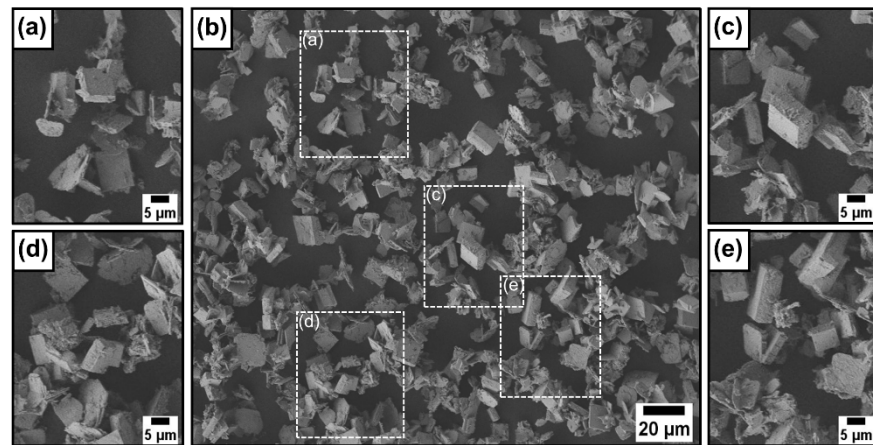


**Figure 12.** (a–e) SEM micrographs of plate-like LNO, gained via SGS-MFS under reaction conditions used in this work. See Table 3 for more information on the experiment parameters. The crystals are about 10  $\mu\text{m}$  long and 2  $\mu\text{m}$  thick. Therefore, the aspect ratio is approximately 5. To determine the length and thickness, 100 particles were analyzed with ImageJ [44]. Figure A12 demonstrates the histograms of the length, thickness and aspect-ratio distribution of the LNO particles.

The chemical composition of one LNO crystal was determined by EDXS. The results of this study are reported in Figure 13 and Table 4. As the basis for the EDXS analysis, the SEM micrograph in Figure 13a was utilized. The EDXS spectrum in Figure 13b affirms the presence of La, Ni and O in the reaction product. As can be seen in Figure 13c–e, the EDXS elemental maps demonstrate that the LNO plate is homogeneously composed of La, Ni and O. Moreover, the La/Ni ratio was calculated to be close to 2:1, which coincides with the stoichiometry of LNO (see Table 4).

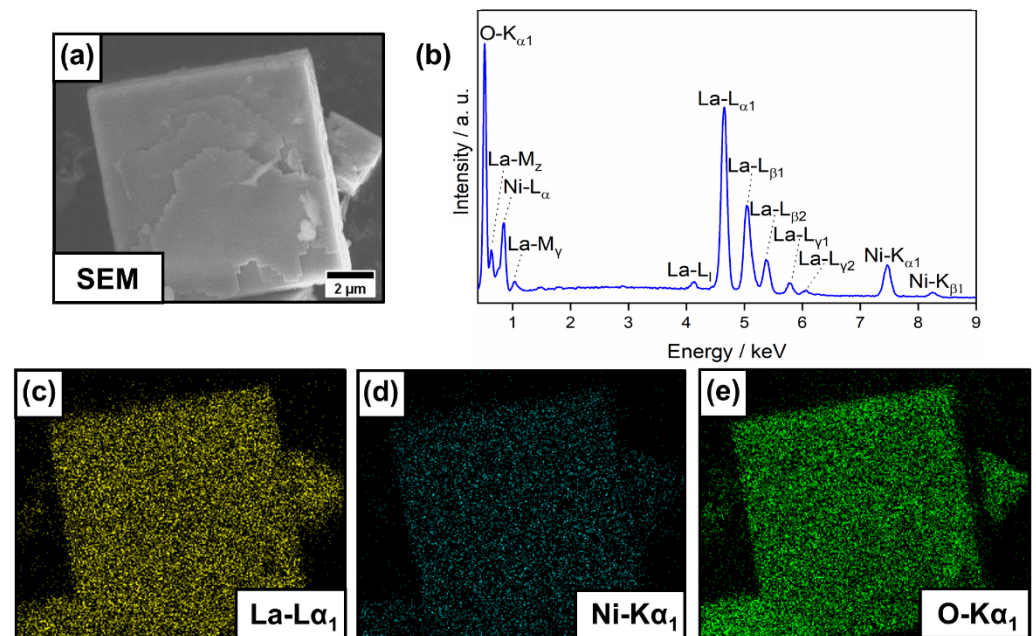


**Figure 13.** EDXS analysis of one LNO crystal, formed via SGS-based MFS using reaction conditions of Table 3: (a) SEM micrograph of plate-like LNO as the basis for EDXS investigations; (b) EDXS spectrum reveals the presence of La, Ni and O in the crystal; (c–e) EDXS elemental maps of La (yellow), Ni (cyan) and O (green) exhibiting homogenous distributions of these elements in the product powder.

**Table 4.** Metal composition of LNO based on EDXS results.

Element	Atomic Percent (%)	Stoichiometric Ratio <sup>1</sup>
La	66.89 ± 0.41	2.02 ± 0.01
Ni	33.11 ± 0.97	1.00 ± 0.03

<sup>1</sup> Normalized by atomic percent of Ni.

#### 4. Conclusions

Plate-like LNO was successfully prepared from MFS using NaOH powder as the flux. The intermediates from a sol–gel process, which were identified as an ultrafine mixture of La<sub>2</sub>O<sub>2</sub>CO<sub>3</sub> and NiO, served as the starting material. Compared with the classical SGP, MFS allows for LNO formation at a lower temperature (starting at 673 K). The influence of different reaction parameters on the synthesis of LNO was investigated. It was found that a La/Ni molar ratio in the sol–gel intermediates of 2:1.15, a sol–gel-intermediates/NaOH-weight ratio of 1:5, the use of a nickel crucible as the reaction vessel and the addition of excess water are conducive to the production of LNO with well-defined plate-like morphology and the highest purity. The length and thickness of the particles averaged 9 μm and 2 μm, respectively, corresponding to an aspect ratio of approximately 5. Even larger crystals can be generated by increasing the reaction time. By choosing these conditions, the undesired La(OH)<sub>3</sub> formation was suppressed. Nevertheless, traces of LaNiO<sub>3</sub> and NiO were still observed, which can be explicated by the increased nickel content in the precursor and the involvement of the wall and bottom of the Ni crucible. Due to their plate-like morphology, LNO crystals can be used in promising future applications.

**Author Contributions:** Conceptualization, G.E.C., Z.Z. and A.F.; methodology, G.E.C. and Z.Z.; validation, G.E.C. and A.F.; formal analysis, G.E.C. and Y.B.; investigation, G.E.C., Y.B. and P.A.K.; resources, A.F.; data curation, G.E.C. and Y.B.; writing—original draft preparation, G.E.C.; writing—review and editing, G.E.C., Y.B., Z.Z., P.A.K. and A.F.; visualization, G.E.C. and Y.B.; supervision, A.F.; project administration, A.F.; funding acquisition, A.F. All authors have read and agreed to the published version of the manuscript.

**Funding:** This research was funded by the Deutsche Forschungsgemeinschaft (DFG, German Research Foundation)—project number 435833397.

**Institutional Review Board Statement:** Not applicable.

**Informed Consent Statement:** Not applicable.

**Data Availability Statement:** Not applicable.

**Acknowledgments:** The authors gratefully appreciate the technical assistance of Frank Steinbach.

**Conflicts of Interest:** The authors declare no conflict of interest.



## Appendix A. Synthesis of Precursors via Sol–Gel Process

### EDXS Analysis of Sol–Gel Intermediates

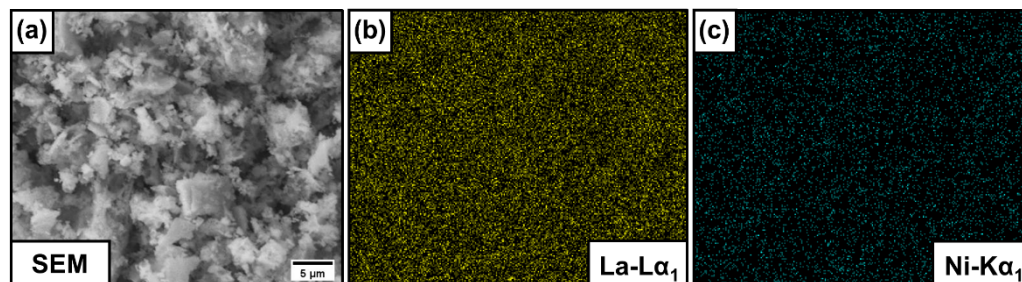


**Figure A1.** (a) SEM micrograph exhibiting selected area for EDXS investigation. EDXS elemental maps of (b) La and (c) Ni confirm homogenous distributions of these elements in sol–gel intermediates.

## Appendix B. Molten-Flux Synthesis of Plate-like $\text{La}_2\text{NiO}_{4+\delta}$ Particles

### Appendix B.1. Influence of Water Amount on MFS of LNO

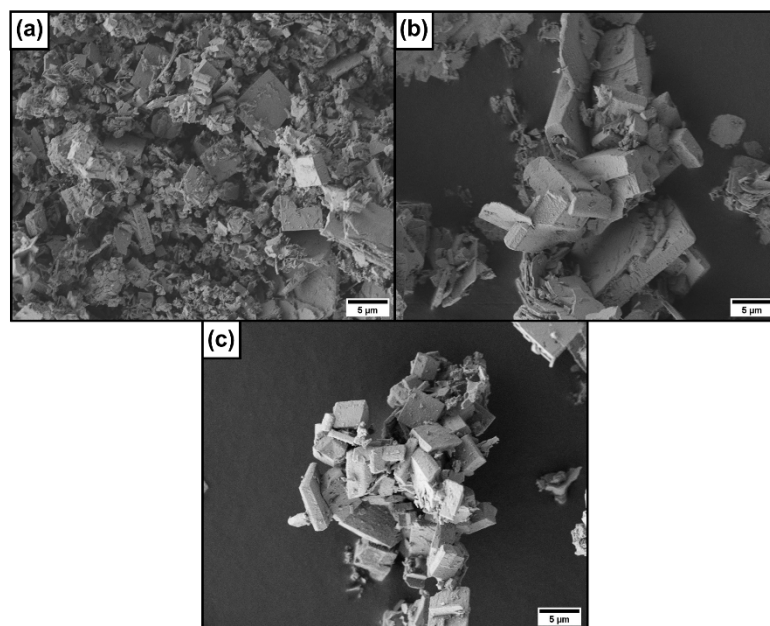


**Figure A2.** SEM micrographs showing the result of MFS with and without the addition of water: (a) when no water was added, plate-like LNO crystals with a length of 3.0 μm and a thickness of 0.5 μm were obtained; (b) the addition of water (NaOH/water-mass ratio = 1:0.1) led to larger plates, the length and thickness of which were about 6.0 μm and 0.7 μm, respectively; (c) doubling the water content (NaOH/water-mass ratio = 1:0.2) resulted in further growth of the particles, so that the LNO plates were 9.0 μm long and 0.8 μm thick.

### Appendix B.2. Role of Reaction Time on MFS of LNO

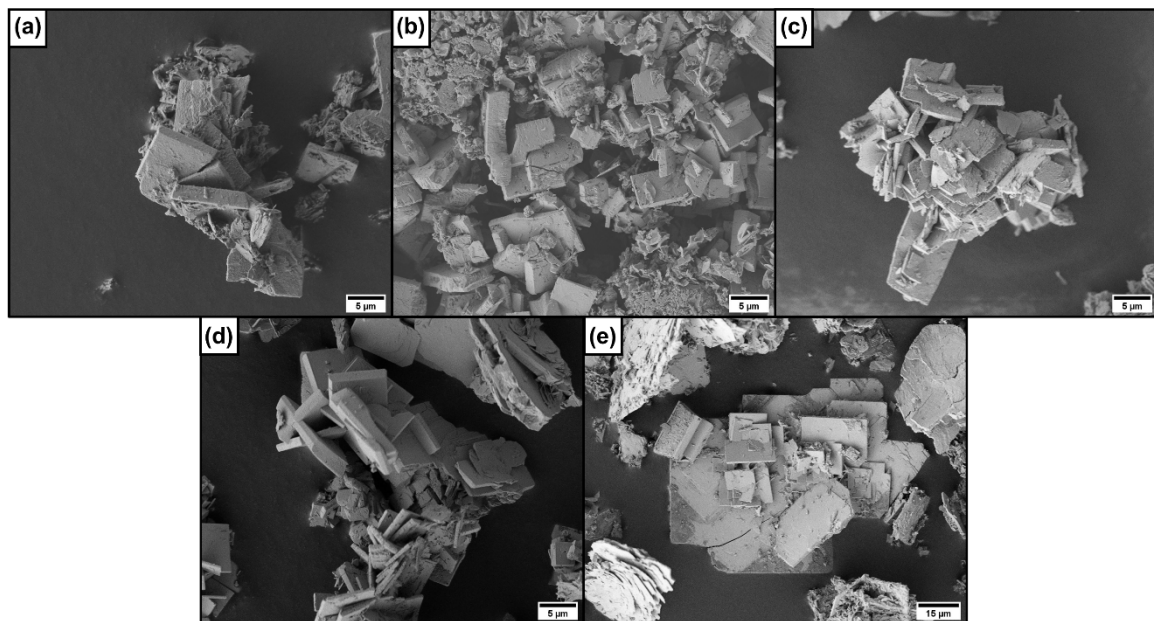


**Figure A3.** SEM micrographs exhibiting reaction products of MFS at 673 K after (a) 6 h; (b) 8 h; (c) 10 h; (d) 12 h; (e) 18 h. (a) After a synthesis time of 6h, LNO crystals with a length of 5.0  $\mu\text{m}$  and thickness of 0.6  $\mu\text{m}$  were formed. By incrementing the reaction time to (b) 8 h, (c) 10 h or (d) 12 h, slight increases in the particle size were recorded (6.0  $\mu\text{m}$   $\times$  0.7  $\mu\text{m}$  for 8 h; 6.40  $\mu\text{m}$   $\times$  0.72  $\mu\text{m}$  for 10 h; 6.8  $\mu\text{m}$   $\times$  0.74  $\mu\text{m}$  for 12 h). (e) The reaction time of 18 h resulted in longer LNO crystals that were 13.0  $\mu\text{m}$  long and 1.8  $\mu\text{m}$  thick.

### Appendix B.3. Effect of Crucible Material on Synthesis of LNO

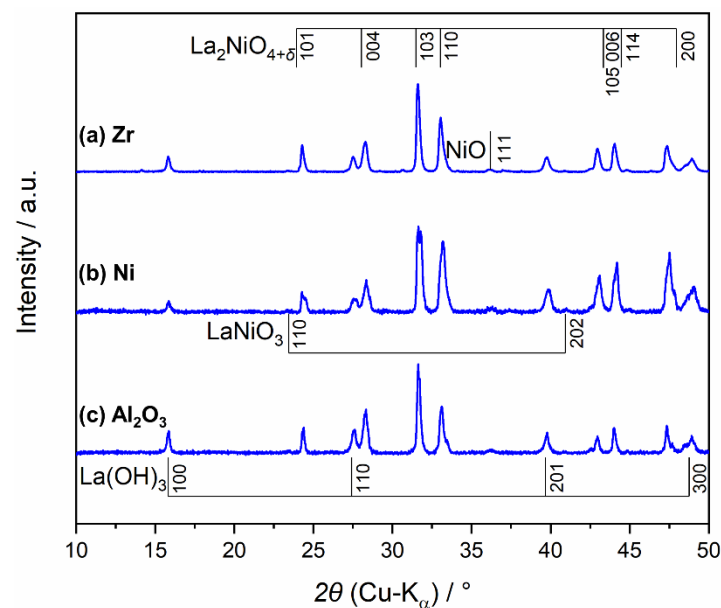


**Figure A4.** XRD patterns exhibiting results of SGS-based MFS in (a) Zr, (b) Ni and (c)  $\text{Al}_2\text{O}_3$  crucibles. Irrespective of the reaction container, tetragonal LNO (PDF 01-089-3589) was obtained as the main phase, accompanied by the minor-phases hexagonal  $\text{La}(\text{OH})_3$  (PDF 01-079-5398) and cubic NiO (PDF 01-071-4750). Using a Ni melting pot, the formation of cubic  $\text{LaNiO}_3$  perovskite (PDF 00-033-0710) was also observed. The XRD data are normalized to the 103 reflection of LNO.

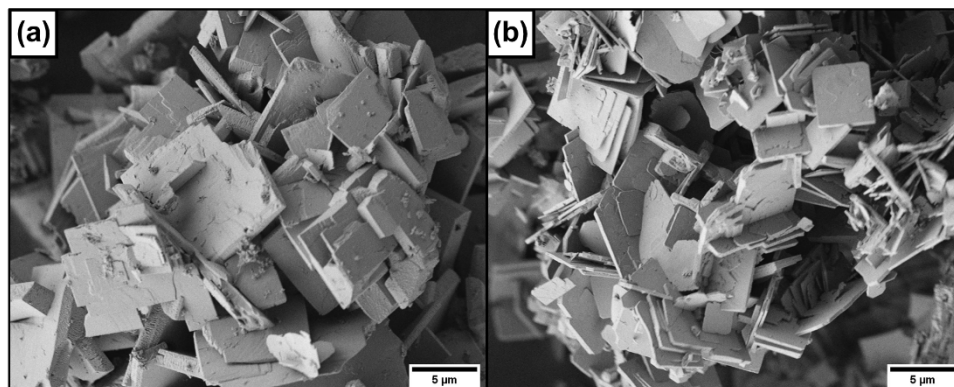


**Figure A5.** SEM micrographs showing plate-like crystals obtained in (a) Zr and (b) Ni crucibles by MFS. For comparison, see SEM micrograph in A3b of LNO plates, produced in an  $\text{Al}_2\text{O}_3$  melting pot. The particle dimensions are  $6.0\ \mu\text{m} \times 0.7\ \mu\text{m}$  ( $\text{Al}_2\text{O}_3$  crucible),  $5.5\ \mu\text{m} \times 0.5\ \mu\text{m}$  (Ni crucible) and  $7.00\ \mu\text{m} \times 0.72\ \mu\text{m}$  (Zr crucible).

#### Appendix B.4. Influence of Reaction Temperature on Synthesis of LNO by MFS

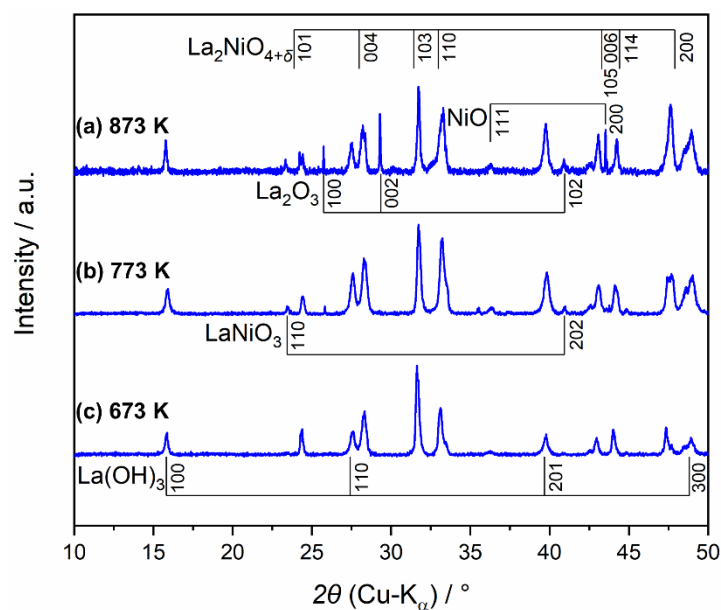


**Figure A6.** XRD patterns show reflections of reaction products, synthesized at (a) 873 K; (b) 773 K; (c) 673 K. Regardless of the chosen temperature, tetragonal LNO (PDF 01-089-3589) was formed as the main product. At temperatures above 673 K, the formation of the secondary phases hexagonal  $\text{La}(\text{OH})_3$  (PDF 01-079-5398), cubic  $\text{LaNiO}_3$  (PDF 00-033-0710), hexagonal  $\text{La}_2\text{O}_3$  (PDF 01-074-2430) and cubic NiO (PDF 01-071-4750) were registered. The XRD data are normalized to the 103 reflection of LNO.

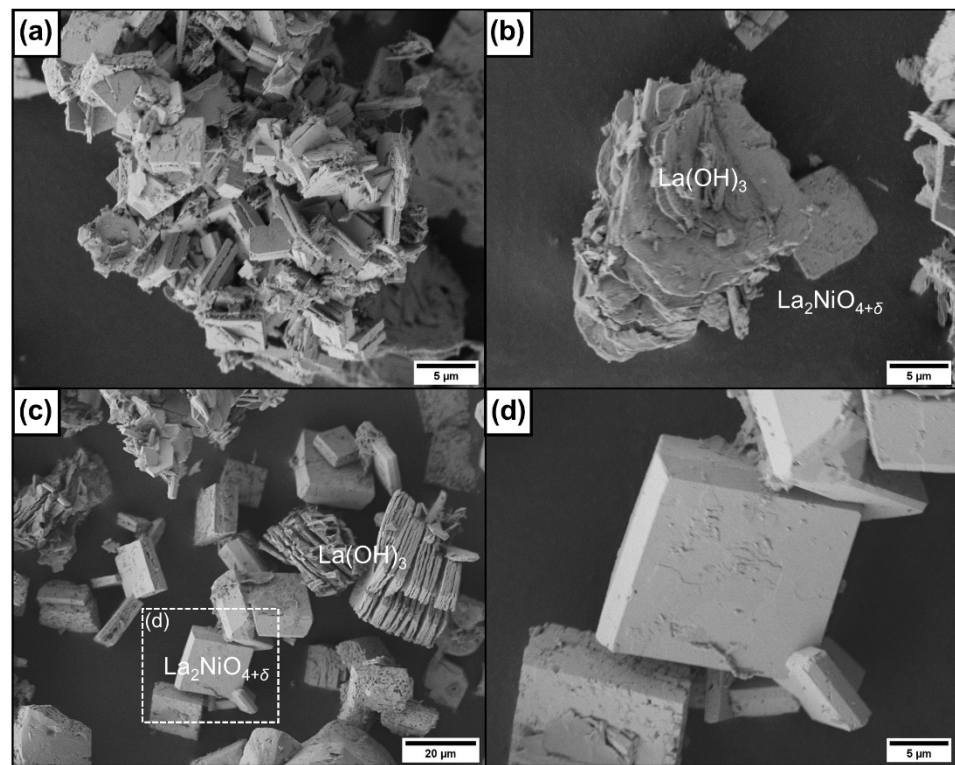


**Figure A7.** SEM micrographs of products obtained at (a,b) 773 K and (c,d) 873 K. Compared with the MFS at 673 K (see Figure A3b), the syntheses at higher temperatures enabled the formation of well-defined LNO plates up to 30  $\mu\text{m}$  in length and up to 2  $\mu\text{m}$  in thickness. However, large layered hexagonal  $\text{La}(\text{OH})_3$  particles with a length of up to 70  $\mu\text{m}$  were identified.

#### Appendix B.5. Importance of NaOH Amount in MFS of LNO

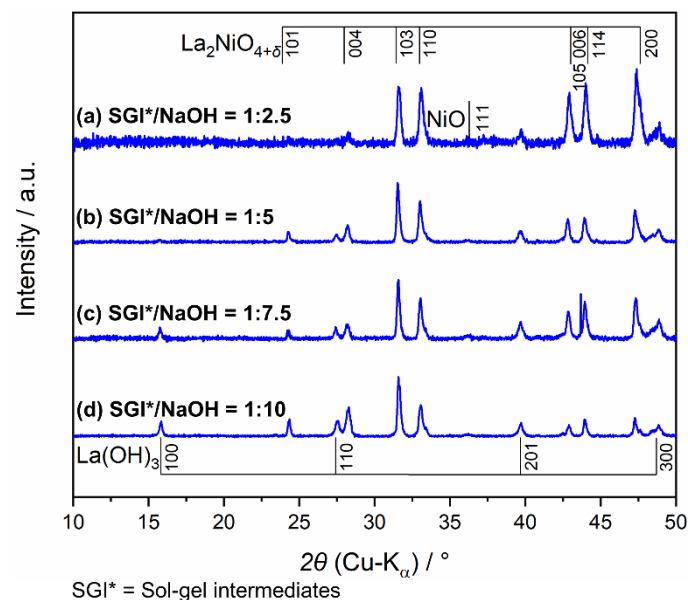


**Figure A8.** XRD measurements performed on reaction products gained with sol-gel-intermediates/NaOH-weight ratios of (a) 1:2.5; (b) 1:5; (c) 1:7.5; (d) 1:10. All XRD patterns affirm the presence of tetragonal LNO (PDF 01-089-3589) as the main phase, as well as hexagonal  $\text{La}(\text{OH})_3$  (PDF 01-079-5398) and cubic NiO (PDF 01-071-4750) as the secondary products. With the increasing NaOH content, the reflections of the  $\text{La}(\text{OH})_3$  became more obvious. The XRD data are normalized to the 103 reflection of LNO.

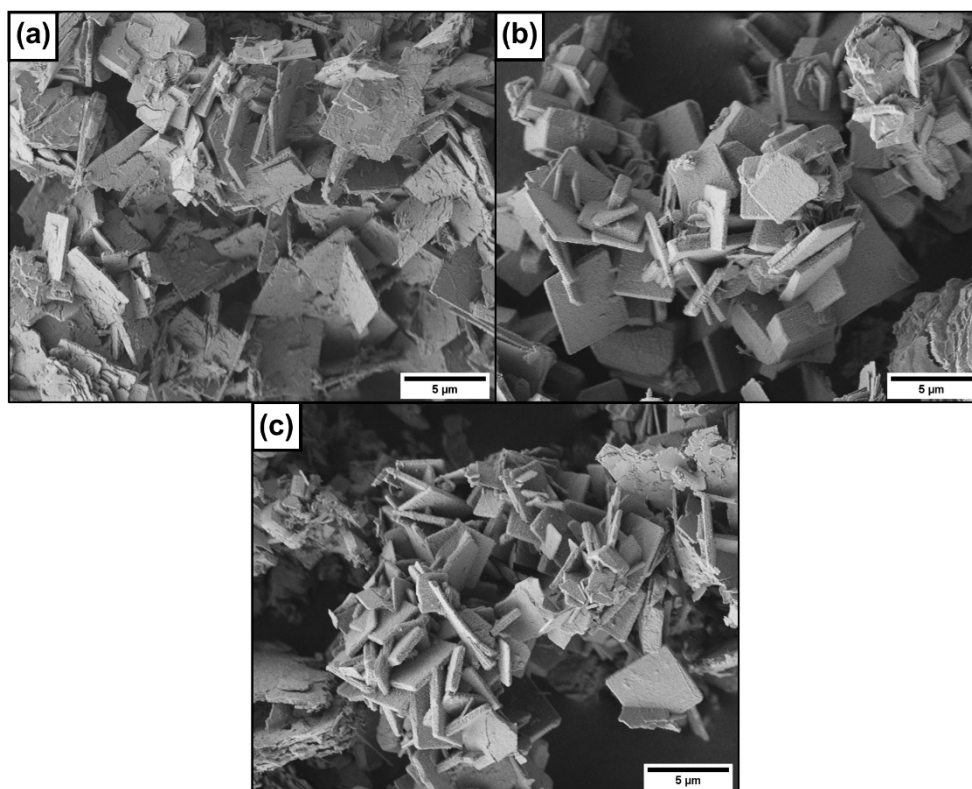


**Figure A9.** SEM micrographs showing morphology of LNO crystals obtained by MFS with sol-gel-intermediates/NaOH-mass ratios of (a) 1:2.5; (b) 1:5; (c) 1:7.5. For a ratio of 1:10, see Figure A3b. All syntheses produced plate-shaped LNO particles. At a ratio of 1:2.5, the plates are partly thin and have a rough structure.

#### Appendix B.6. Impact of La/Ni Molar Ratio in Sol-Gel Intermediates on LNO Synthesis

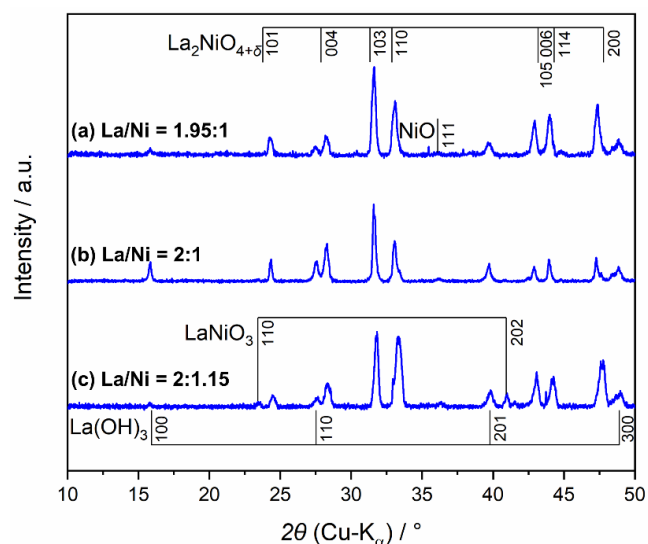


**Figure A10.** XRD patterns displaying the reflections of the obtained reaction products in an  $\text{Al}_2\text{O}_3$  crucible when the La/Ni ratio in the reactant mixture was (a) 1.95:1; (b) 2:1; (c) 2:1.15. Regardless of the La/Ni ratio employed, the main product formed was tetragonal LNO (PDF 01-089-3589), accompanied by the secondary phases hexagonal  $\text{La}(\text{OH})_3$  (PDF 01-079-5398) and cubic NiO (PDF 01-071-4750). By using a higher Ni amount in the sol-gel powder,  $\text{LaNiO}_3$  reflections (PDF 00-033-0710) were also found. The XRD data are normalized to the 103 reflection of LNO.

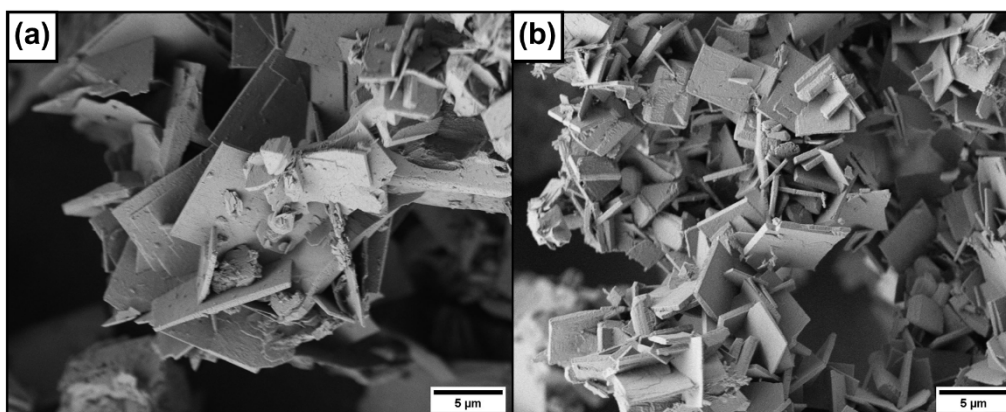


**Figure A11.** SEM micrographs of the reaction products, gained by MFS using La/Ni molar ratios in the sol–gel intermediates of (a) 1.95:1 and (b) 2:1.15. For a La/Ni ratio of 2:1, see the SEM image in Figure A3b. All syntheses produced plate-like LNO crystals.

#### Appendix B.7. Determination of Dimensions of LNO Crystals

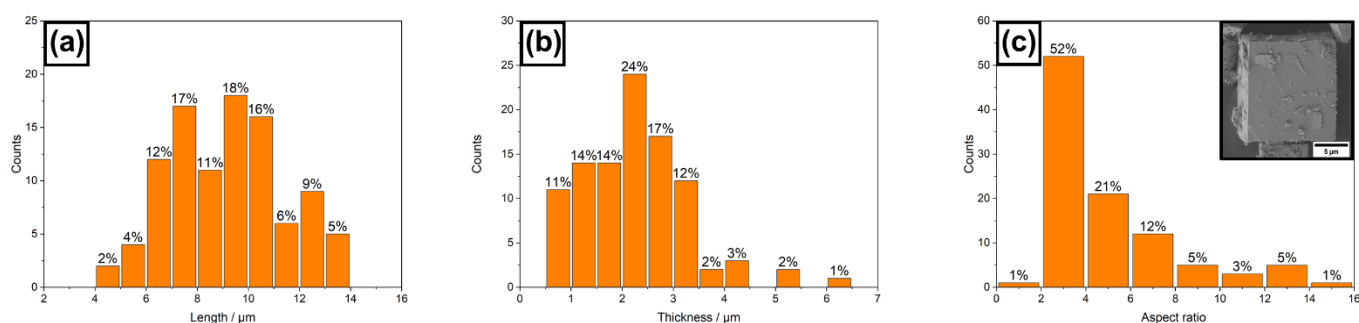


**Figure A12.** Histograms of (a) length, (b) thickness and (c) aspect-ratio distribution of LNO particles obtained by SGS–MFS using reaction conditions from Table 3. The inset in (c) illustrates the SEM micrograph of a typical plate-like LNO crystal. A total of 100 particles were analyzed with ImageJ [44] to create the histograms.

## References

- Klande, T.; Efimov, K.; Cusenza, S.; Becker, K.D.; Feldhoff, A. Effect of doping, microstructure, and CO<sub>2</sub> on La<sub>2</sub>NiO<sub>4+δ</sub>-based oxygen-transporting materials. *J. Solid State Chem.* **2011**, *184*, 3310–3318. [CrossRef]
- Liang, F.; Jiang, H.; Luo, H.; Caro, J.; Feldhoff, A. Phase stability and permeation behavior of a dead-end Ba<sub>0.5</sub>Sr<sub>0.5</sub>Co<sub>0.8</sub>Fe<sub>0.2</sub>O<sub>3-δ</sub> tube membrane in high-purity oxygen production. *Chem. Mater.* **2011**, *23*, 4765–4772. [CrossRef]
- Kondratenko, E.V.; Wang, H.; Kondratenko, V.A.; Caro, J. Selective oxidation of CH<sub>4</sub> and C<sub>2</sub>H<sub>6</sub> over a mixed oxygen ion and electron conducting perovskite—A TAP and membrane reactors study. *J. Mol. Catal. A Chem.* **2009**, *297*, 142–149. [CrossRef]
- Jiang, H.; Wang, H.; Werth, S.; Schiestel, T.; Caro, J. Simultaneous production of hydrogen and synthesis gas by combining water splitting with partial oxidation of methane in a hollow-fiber membrane reactor. *Angew. Chemie. Int. Ed.* **2008**, *47*, 9341–9344. [CrossRef] [PubMed]
- Jeong, C.; Lee, J.H.; Park, M.; Hong, J.; Kim, H.; Son, J.W.; Lee, J.H.; Kim, B.K.; Yoon, K.J. Design and processing parameters of La<sub>2</sub>NiO<sub>4+δ</sub>-based cathode for anode-supported planar solid oxide fuel cells (SOFCs). *J. Power Sources* **2015**, *297*, 370–378. [CrossRef]
- Ma, Z.; Yuan, X.; Li, L.; Ma, Z.F.; Wilkinson, D.P.; Zhang, L.; Zhang, J. A review of cathode materials and structures for rechargeable lithium-air batteries. *Energy Environ. Sci.* **2015**, *8*, 2144–2198. [CrossRef]
- Chen, G.; Feldhoff, A.; Weidenkaff, A.; Li, C.; Liu, S.; Zhu, X.; Sunarso, J.; Huang, K.; Wu, X.Y.; Ghoniem, A.F.; et al. Roadmap for sustainable mixed ionic-electronic conducting membranes. *Adv. Funct. Mater.* **2022**, *32*, 2105702. [CrossRef]
- Chroneos, A.; Parfitt, D.; Kilner, J.A.; Grimes, R.W. Anisotropic oxygen diffusion in tetragonal La<sub>2</sub>NiO<sub>4+δ</sub>: Molecular dynamics calculations. *J. Mater. Chem.* **2010**, *20*, 266–270. [CrossRef]
- Naumovich, E.N.; Kharton, V.V. Atomic-scale insight into the oxygen ionic transport mechanisms in La<sub>2</sub>NiO<sub>4</sub>-based materials. *J. Mol. Struct. Theochem.* **2010**, *946*, 57–64. [CrossRef]

10. Sayers, R.; De Souza, R.A.; Kilner, J.A.; Skinner, S.J. Low temperature diffusion and oxygen stoichiometry in lanthanum nickelate. *Solid State Ion.* **2010**, *181*, 386–391. [[CrossRef](#)]
11. Bassat, J.M.; Odier, P.; Villesuzanne, A.; Marin, C.; Pouchard, M. Anisotropic ionic transport properties in  $\text{La}_2\text{NiO}_{4+\delta}$  single crystals. *Solid State Ion.* **2004**, *167*, 341–347. [[CrossRef](#)]
12. Bassat, J.M.; Burriel, M.; Wahyudi, O.; Castaing, R.; Ceretti, M.; Veber, P.; Weill, I.; Villesuzanne, A.; Grenier, J.C.; Paulus, W.; et al. Anisotropic oxygen diffusion properties in  $\text{Pr}_2\text{NiO}_{4+\delta}$  and  $\text{Nd}_2\text{NiO}_{4+\delta}$  single crystals. *J. Phys. Chem. C* **2013**, *117*, 26466–26472. [[CrossRef](#)]
13. Kharton, V.V.; Viskup, A.P.; Naumovich, E.N.; Marques, F.M.B. Oxygen ion transport in  $\text{La}_2\text{NiO}_4$ -based ceramics. *J. Mater. Chem.* **1999**, *9*, 2623–2629. [[CrossRef](#)]
14. Skinner, S.J. Characterisation of  $\text{La}_2\text{NiO}_{4+\delta}$  using in-situ high temperature neutron powder diffraction. *Solid State Sci.* **2003**, *5*, 419–426. [[CrossRef](#)]
15. Paulus, W.; Cousson, A.; Dhalenne, G.; Berthon, J.; Revcolevschi, A.; Hosoya, S.; Treutmann, W.; Heger, G.; Toquin, R.L. Neutron diffraction studies of stoichiometric and oxygen intercalated  $\text{La}_2\text{NiO}_4$  single crystals. *Solid State Sci.* **2002**, *4*, 565–573. [[CrossRef](#)]
16. Tranquada, J.M.; Kong, Y.; Lorenzo, J.E.; Buttrey, D.J.; Rice, D.E.; Sachan, V. Oxygen intercalation, stage ordering, and phase separation in  $\text{La}_2\text{NiO}_{4+\delta}$  with  $0.05 \leq \delta \leq 0.11$ . *Phys. Rev. B* **1994**, *50*, 6340–6351. [[CrossRef](#)] [[PubMed](#)]
17. Efimov, K.; Arnold, M.; Martynczuk, J.; Feldhoff, A. Crystalline intermediate phases in the sol-gel-based synthesis of  $\text{La}_2\text{NiO}_{4+\delta}$ . *J. Am. Ceram. Soc.* **2009**, *92*, 876–880. [[CrossRef](#)]
18. Fontaine, M.L.; Laberty-Robert, C.; Ansart, F.; Tailhades, P. Elaboration and characterization of  $\text{La}_2\text{NiO}_{4+\delta}$  powders and thin films via a modified sol-gel process. *J. Solid State Chem.* **2004**, *177*, 1471–1479. [[CrossRef](#)]
19. Boumaza, S.; Brahim, R.; Boudjellal, L.; Belhadi, A.; Trari, M. Photoelectrochemical study of  $\text{La}_2\text{NiO}_4$  synthesized using citrate sol gel method-application for hydrogen-production. *J. Solid State Electrochem.* **2020**, *24*, 329–337. [[CrossRef](#)]
20. Hao, X.; Ma, C.; Yang, X.; Liu, T.; Wang, B.; Liu, F.; Liang, X.; Yang, C.; Zhu, H.; Lu, G. YSZ-based mixed potential  $\text{H}_2\text{S}$  sensor using  $\text{La}_2\text{NiO}_4$  sensing electrode. *Sens. Actuators B Chem.* **2018**, *255*, 3033–3039. [[CrossRef](#)]
21. Porob, D.G.; Maggard, P.A. Synthesis of textured  $\text{Bi}_5\text{Ti}_3\text{FeO}_{15}$  and  $\text{LaBi}_4\text{Ti}_3\text{FeO}_{15}$  ferroelectric layered Aurivillius phases by molten-salt flux methods. *Mater. Res. Bull.* **2006**, *41*, 1513–1519. [[CrossRef](#)]
22. Li, Z.; Zhang, X.; Hou, J.; Zhou, K. Molten salt synthesis of anisometric  $\text{Sr}_3\text{Ti}_2\text{O}_7$  particles. *J. Cryst. Growth* **2007**, *305*, 265–270. [[CrossRef](#)]
23. Elwell, D.; Neate, B.W. Mechanisms of crystal growth from fluxed melts. *J. Mater. Sci.* **1971**, *6*, 1499–1519. [[CrossRef](#)]
24. Matei, C.; Berger, D.; Marote, P.; Deloume, J.P. Molten salt synthesis of lanthanum cuprate,  $\text{La}_2\text{CuO}_{4+\delta}$ . *J. Electroceramics* **2010**, *24*, 64–66. [[CrossRef](#)]
25. Boltersdorf, J.; King, N.; Maggard, P.A. Flux-mediated crystal growth of metal oxides: Synthetic tunability of particle morphologies, sizes, and surface features for photocatalysis research. *CrystEngComm* **2015**, *17*, 2225–2241. [[CrossRef](#)]
26. Ueno, S.; Sakamoto, Y.; Taguchi, H.; Nakashima, K.; Wada, S. Microstructures of lanthanum nickel oxide particles with crystal facets synthesized in molten chlorides. *J. Ceram. Soc. Jpn.* **2015**, *123*, 351–354. [[CrossRef](#)]
27. Schober, T. Composites of ceramic high-temperature proton conductors with inorganic compounds. *Electrochem. Solid-State Lett.* **2005**, *8*, 199–201. [[CrossRef](#)]
28. Shivakumara, C.; Hegde, M.S.; Prakash, A.S.; Khadar, A.M.A.; Subbanna, G.N.; Lalla, N.P. Low temperature synthesis, structure and properties of alkali-doped  $\text{La}_2\text{NiO}_4$ ,  $\text{LaNiO}_3$  and  $\text{LaNi}_{0.85}\text{Cu}_{0.15}\text{O}_3$  from alkali hydroxide fluxes. *Solid State Sci.* **2003**, *5*, 351–357. [[CrossRef](#)]
29. Flood, H.; Förland, T. The acidic and basic properties of oxides. *Acta. Chem. Scand.* **1947**, *1*, 592–604. [[CrossRef](#)]
30. Matei, C.; Berger, D.; Marote, P.; Stoleriu, S.; Deloume, J.P. Lanthanum-based perovskites obtained in molten nitrates or nitrites. *Prog. Solid. State. Chem.* **2007**, *35*, 203–209. [[CrossRef](#)]
31. Liu, X.; Fechner, N.; Antonietti, M. Salt melt synthesis of ceramics, semiconductors and carbon nanostructures. *Chem. Soc. Rev.* **2013**, *42*, 8237–8265. [[CrossRef](#)]
32. Janz, G.J. Molten carbonate electrolytes as acid-base solvent systems. *J. Chem. Educ.* **1967**, *44*, 581. [[CrossRef](#)]
33. Radtke, V.; Himmel, D.; Pütz, K.; Goll, S.K.; Krossing, I. The electrochemical potential map (PPM): An absolute two-dimensional chemical potential scale for a global understanding of chemistry. *Chem. Eur. J.* **2014**, *20*, 4194–4211. [[CrossRef](#)] [[PubMed](#)]
34. Ham, W.K.; Holland, G.F.; Stacy, A.M. Low-temperature synthesis of superconducting  $\text{La}_{2-x}\text{M}_x\text{CuO}_4$ : Direct precipitation from  $\text{NaOH/KOH}$  melts. *J. Am. Chem. Soc.* **1988**, *110*, 5214–5215. [[CrossRef](#)]
35. Marquez, L.N.; Keller, S.W.; Stacy, A.M.; Fendorf, M.; Gronsky, R. Synthesis of twin-free, orthorhombic  $\text{EuBa}_2\text{Cu}_3\text{O}_{7-\delta}$  superconductors at 450 °C by direct precipitation from molten  $\text{NaOH}$  and  $\text{KOH}$ . *Chem. Mater.* **1993**, *5*, 761–764. [[CrossRef](#)]
36. Luce, J.L.; Stacy, A.M. Crystallization of  $\text{LnCu}_2\text{O}_4$  ( $\text{Ln} = \text{La, Nd, Sm, Eu, Gd, Dy, Ho, Y, Er}$ ) from hydroxide melts: Synthesis and structure. *Chem. Mater.* **1997**, *9*, 1508–1515. [[CrossRef](#)]
37. Shivakumara, C. Low temperature synthesis and characterization of rare earth orthoferrites  $\text{LnFeO}_3$  ( $\text{Ln} = \text{La, Pr and Nd}$ ) from molten  $\text{NaOH}$  flux. *Solid State Commun.* **2006**, *139*, 165–169. [[CrossRef](#)]
38. Shivakumara, C.; Hedge, M.S. Low temperature synthesis of layered  $\text{Na}_x\text{CoO}_2$  and  $\text{K}_x\text{CoO}_2$  from  $\text{NaOH/KOH}$  fluxes and their ion exchange properties. *J. Chem. Sci.* **2003**, *115*, 447–457. [[CrossRef](#)]
39. Hinterding, R.; Zhao, Z.; Zhang, C.; Feldhoff, A. Anisotropic growth of  $\text{La}_2\text{NiO}_{4+\delta}$ : Influential pre-treatment in molten-flux synthesis. *J. Cryst. Growth* **2019**, *523*, 125135. [[CrossRef](#)]

40. Seabaugh, M.M.; Cheney, G.L.; Hasinska, K.; Azad, A.B.; Sabolsky, E.M.; Swartz, S.L.; Dawson, W.J. Development of a templated grain growth system for texturing piezoelectric ceramics. *J. Intell. Mater. Syst. Struct.* **2004**, *15*, 209–214. [CrossRef]
41. Hinterding, R.; Zhao, Z.; Wolf, M.; Jakob, M.; Oeckler, O.; Feldhoff, A. Ceramic composites based on  $\text{Ca}_3\text{Co}_{4-x}\text{O}_{9+\delta}$  and  $\text{La}_2\text{NiO}_{4+\delta}$  with enhanced thermoelectric properties. *Open Ceram.* **2021**, *6*, 100103. [CrossRef]
42. Kimura, T. Microstructure development and texture formation in lead-free piezoelectric ceramics prepared by templated grain growth process. *J. Ceram. Soc. Jpn.* **2016**, *124*, 268–282. [CrossRef]
43. Ma, X.; Wang, B.; Xhafa, E.; Sun, K.; Nikolla, E. Synthesis of shape-controlled  $\text{La}_2\text{NiO}_{4+\delta}$  nanostructures and their anisotropic properties for oxygen diffusion. *Chem. Commun.* **2015**, *51*, 137–140. [CrossRef]
44. Schneider, C.A.; Rasband, W.S.; Eliceiri, K.W. NIH Image to ImageJ: 25 years of image analysis. *Nat. Methods* **2012**, *9*, 671–675. [CrossRef] [PubMed]
45. Feldhoff, A.; Arnold, M.; Martynczuk, J.; Gesing, T.M.; Wang, H. The sol-gel synthesis of perovskites by an EDTA/citrate complexing method involves nanoscale solid state reactions. *Solid State Sci.* **2008**, *10*, 689–701. [CrossRef]
46. Feldhoff, A.; Martynczuk, J.; Wang, H. Advanced  $\text{Ba}_{0.5}\text{Sr}_{0.5}\text{Zn}_{0.2}\text{Fe}_{0.8}\text{O}_{3-\delta}$  perovskite-type ceramics as oxygen selective membranes: Evaluation of the synthetic process. *Prog. Solid. State Chem.* **2007**, *35*, 339–353. [CrossRef]
47. Bangruwa, J.S.; Kumar, S.; Chauhan, A.; Kumar, P.; Verma, V. Modified magnetic and electrical properties of perovskite-spinel multiferroic composites. *J. Supercond. Nov. Magn.* **2019**, *32*, 2559–2569. [CrossRef]
48. Theingi, M.; Tun, K.T.; Aung, N.N. Preparation, characterization and optical Property of  $\text{LaFeO}_3$  nanoparticles via sol-gel combustion method. *SciMed. J.* **2019**, *1*, 151–157. [CrossRef]
49. Mentus, S.; Jelić, D.; Grudić, V. Lanthanum nitrate decomposition by both temperature programmed heating and citrate gel combustion. *J. Therm. Anal. Calorim.* **2007**, *90*, 393–397. [CrossRef]
50. Schott, G.; Davidson, N. Shock waves in chemical kinetics: The decomposition of  $\text{N}_2\text{O}_5$  at high Temperatures. *J. Am. Chem. Soc.* **1958**, *80*, 1841–1853. [CrossRef]
51. Martynczuk, J.; Arnold, M.; Wang, H.; Caro, J.; Feldhoff, A. How  $(\text{Ba}_{0.5}\text{Sr}_{0.5})(\text{Fe}_{0.8}\text{Zn}_{0.2})\text{O}_{3-\delta}$  and  $(\text{Ba}_{0.5}\text{Sr}_{0.5})(\text{Co}_{0.8}\text{Fe}_{0.2})\text{O}_{3-\delta}$  perovskites form via an EDTA/citric acid complexing method. *Adv. Mater.* **2007**, *19*, 2134–2140. [CrossRef]
52. Gao, X.; Fisher, C.A.J.; Kimura, T.; Ikuhara, Y.H.; Kuwabara, A.; Moriwake, H.; Oki, H.; Tojigamori, T.; Kohama, K.; Ikuhara, Y. Domain boundary structures in lanthanum lithium titanates. *J. Mater. Chem. A* **2014**, *2*, 843–852. [CrossRef]
53. Castro, F.C.; Li, Q.; Evmenenko, G.; Buchholz, D.B.; Wu, J.; Bedzyk, M.; Dravid, V.P. Dynamics of electrochemical conversion of nanoscale metal-metal oxide multilayer architecture. *Microsc. Microanal.* **2016**, *22*, 1316–1317. [CrossRef]
54. EELS. Info. Available online: <https://eels.info/atlas> (accessed on 10 June 2022).
55. Xue, J.; Feldhoff, A. Ambient air partial internal reduction of NiO in a mixed ionic-electronic conducting ceramic. *J. Eur. Ceram. Soc.* **2016**, *36*, 3451–3456. [CrossRef]
56. Kan, Y.; Jin, X.; Wang, P.; Li, Y.; Cheng, Y.B.; Yan, D. Anisotropic grain growth of  $\text{Bi}_4\text{Ti}_3\text{O}_{12}$  in molten salt fluxes. *Mater. Res. Bull.* **2003**, *38*, 567–576. [CrossRef]
57. Orum, A.; Takatori, K.; Hori, S.; Ikeda, T.; Yoshimura, M.; Tani, T. Atomic force microscopy surface analysis of layered perovskite  $\text{La}_2\text{Ti}_2\text{O}_7$  particles grown by molten flux method. *Jpn. J. Appl. Phys.* **2016**, *55*, 08NB08. [CrossRef]
58. Lad, R.A.; Sidney, L.S. A study of corrosion and mass transfer of nickel by molten sodium hydroxide. *Corrosion* **1954**, *10*, 435–439. [CrossRef]
59. Komath, M. Hot corrosion of nickel in anhydrous sodium hydroxide. *Mater. Chem. Phys.* **1996**, *45*, 171–175. [CrossRef]
60. Williams, D.D.; Grand, J.A.; Miller, R.R. The reactions of molten sodium hydroxide with various metals. *J. Am. Chem. Soc.* **1956**, *78*, 5150–5155. [CrossRef]
61. Li, L.; Deng, J.; Chen, J.; Xing, X. Topochemical molten salt synthesis for functional perovskite compounds. *Chem. Sci.* **2016**, *7*, 855–865. [CrossRef]
62. Yoon, K.H.; Cho, Y.S.; Kang, D.H. Molten salt synthesis of lead-based relaxors. *J. Mater. Sci.* **1998**, *33*, 2977–2984. [CrossRef]
63. Gupta, S.K.; Mao, Y. A review on molten salt synthesis of metal oxide nanomaterials: Status, opportunity, and challenge. *Prog. Mater. Sci.* **2021**, *117*, 100734. [CrossRef]
64. Kimura, T. Chapter 4. Molten Salt Synthesis of Ceramic Powders. In *Advances in Ceramics-Synthesis and Characterization, Processing and Specific Applications*; Sikalidis, C., Ed.; INTECH: Rijeka, Croatia, 2011; pp. 75–100. [CrossRef]
65. Vinothkumar, G.; Rengaraj, S.; Arunkumar, P.; Cha, S.W.; Suresh Babu, K. Ionic radii and concentration dependency of  $\text{RE}^{3+}$  ( $\text{Eu}^{3+}$ ,  $\text{Nd}^{3+}$ ,  $\text{Pr}^{3+}$ , and  $\text{La}^{3+}$ )-doped cerium oxide nanoparticles for enhanced multienzyme-mimetic and hydroxyl radical scavenging activity. *J. Phys. Chem. C* **2019**, *123*, 541–553. [CrossRef]
66. Morris, D.F.C. Ionic radii and enthalpies of hydration of ions. In *Structure and Bonding*; Springer: Berlin/Heidelberg, Germany, 1969; pp. 63–82. [CrossRef]
67. Rabenau, A.; Eckerlin, P. Die  $\text{K}_2\text{NiF}_4$ -Struktur beim  $\text{La}_2\text{NiO}_4$ . *Acta Cryst.* **1958**, *11*, 304–306. [CrossRef]